

# Nuclear and Extended Spectra of NGC 1068 - I: Hints from Near-Infrared Spectroscopy

Lucimara P. Martins<sup>1\*†</sup>, Alberto Rodríguez-Ardila<sup>2†</sup>, Ronaldo de Souza<sup>3</sup>,  
and Ruth Gruenwald<sup>3</sup>

<sup>1</sup>*NAT - Universidade Cruzeiro do Sul, Rua Galvao Bueno, São Paulo, SP, Brazil.*

<sup>2</sup>*Laboratório Nacional de Astrofísica/MCT, Rua dos Estados Unidos 154, Bairro das Nações, CEP 37504-364, Itajubá, MG, Brazil.*

<sup>3</sup>*Instituto Astronômico e Geofísico - USP, Rua do Matão, 1226, São Paulo, SP*

Accepted ? December ? Received ? December ?; in original form ? October ?

## ABSTRACT

We report the first simultaneous zJHK spectroscopy on the archetypical Seyfert 2 Galaxy NGC 1068 covering the wavelength region 0.9 to 2.4  $\mu\text{m}$ . The slit, aligned in the NS direction and centred in the optical nucleus, maps a region 300 pc in radius at sub-arcsec resolution, with a spectral resolving power of 360  $\text{km s}^{-1}$ . This configuration allow us to study the physical properties of the nuclear gas including that of the north side of the ionization cone, map the strong excess of continuum emission in the K-band and attributed to dust and study the variations, both in flux and profile, in the emission lines. Our results show that (1) Mid- to low-ionization emission lines are splitted into two components, whose relative strengths vary with the position along the slit and seem to be correlated with the jet. (2) The coronal lines are single-peaked and are detected only in the central few hundred of parsecs from the nucleus. (3) The absorption lines indicate the presence of intermediate age stellar population, which might be a significant contributor to the continuum in the NIR spectra. (4) Through some simple photoionization models we find photoionization as the main mechanism powering the emitting gas. (5) Calculations using stellar features point to a mass concentration inside the 100 - 200 pc of about  $10^{10} M_{\odot}$ .

## Key words:

Galaxies: active - Galaxies: individual (NGC 1068) - Galaxies: Seyfert - Infrared: galaxies

## 1 INTRODUCTION

Near-IR spectroscopy has been playing a unique role in our understanding of the AGN phenomenon for several reasons. First, it includes a wealth of emission lines and stellar absorption features not observed in the optical, which are useful for studying the physical properties of the emission gas and to determine the age and metallicity of the nuclear stellar population as, for instance, the strong CO bandheads in the H and K bands (e.g., Schreiber 1998; Origlia, Moorwood, & Oliva 1993). Second, extinction by dust is attenuated by a factor of ten relative to that of the optical, allowing to

probe depths unreachable at shorter wavelengths. Third, it is a transition region, where the continuum from the central source no longer dominates while the thermal continuum produced by dust and stars becomes important.

In the last years, the interest for observation in this interval has increased, and thanks to the availability of cross-dispersed (XD) spectrographs, it is possible to study the whole 0.8-2.4  $\mu\text{m}$  region in a single observation, avoiding the aperture and seeing effects that usually affects *JHK* spectroscopy done in long-slit single band observations.

With the above in mind, here we present the first spatially resolved XD spectroscopy covering the interval 0.8-2.4  $\mu\text{m}$  made for NGC1068. This object is one of the nearest and probably the most intensely studied Seyfert 2 galaxy. Observations in all wavelength bands from radio to hard X-rays have formed a uniquely detailed picture of this source. NGC 1068 has played a unique role in the development of unified scenarios for Seyfert 1 and Seyfert 2 galaxies (An-

\* Email: lucimara.martins@cruzeirodosul.edu.br

† Visiting Astronomer at the Infrared Telescope Facility, which is operated by the University of Hawaii under Cooperative Agreement no. NNX-08AE38A with the National Aeronautics and Space Administration, Science Mission Directorate, Planetary Astronomy Program.

tonucci & Miller 1985), in the study of molecular gas in the nuclear region of Seyferts (e.g., Myers & Scoville 1987; Tacconi et al. 1994), and in elucidating the importance of star formation activity coexistent with the active galactic nucleus (AGN), on both larger (e.g., Telesco & Decher 1988) and smaller (Macchetto et al. 1994; Thatte et al. 1997) scales. NGC 1068 also hosts a prominent narrow-line region (NLR) that is approximately co-spatial with a linear radio source with two lobes (Wilson & Ulvestad 1983). The narrow emission line region has been extensively characterized from subarcsecond clouds probed by the Hubble Space Telescope (HST) (Evans et al. 1991; Macchetto et al. 1994) to the ionization cone and extended emission-line region (Pogge 1988; Unger et al. 1992) extending to radii of at least  $30''$  ( $1''=72$  pc at the distance of 14.4 Mpc; Tully 1988).

From approximately  $2''$  southwest to the nucleus to  $4''$  northeast, emission lines exhibit multiple components (Cecil et al. 1990; Crenshaw & Kraemer 2000a). Broad lines were found to be approximately  $2500 - 4000 \text{ km s}^{-1}$  wide, which may be linked to those that are found in polarized light and believed to be reflected light from the inner broad line region (BLR). Narrow lines consist of a pair of red and blue components. Optical studies of [O II] and [N II] line profiles suggest that the separation of these two components varies across the conical NLR. Between  $\sim 2''.5$  and  $4''.5$  northeast from the nucleus, UV line emission is redshifted relative to the systemic value, a pattern that is interpreted as the expansion of the plasma in the radio lobe (Axon et al. 1998).

The mechanisms powering the gas of the NLR, i.e. photoionization from the nucleus or shocks produced by jets, have long been under debate. Dopita & Sutherland (1996) and Bicknell et al. (1998) proposed that the emission in the NLR may be entirely caused by shocks. Velocity splitting over  $1000 \text{ km}^{-1}$ , reported by Axon et al. (1998), in the vicinity of some of the bright emission-line knots provides evidence that fast shocks exist in the NLR of NGC 1068. However, more recent HST data (Crenshaw & Kraemer 2000b; Cecil et al. 2002; Mazzalay et al. 2009) found that the emission line ratios are consistent with photoionization instead of shock heating mechanism. On the other hand, models accounting for both photoionization from the central radiation and shocks were required to explain both the continuum and emission-lines observed in the spectra of active galaxies (e.g., Contini, Rodríguez-Ardila & Viegas 2003, Rodríguez-Ardila, Contini & Viegas 2005).

The scenario in NGC 1068 is thus clearly complex, and observational constraints from all wavelengths need to be put together if we want to understand the processes taking place in this galaxy. Spatially resolved NLR spectroscopy in the NIR can contribute to the solution of the NGC 1068 puzzle. Here, we present the first observations on this source covering simultaneously the  $0.8-2.4 \mu\text{m}$  region at moderate spectral and spatial resolution. Our data are thus able to map a wavelength interval rich in emission lines with a large range of ionization and absorption features from the stellar population not only from the nucleus but also from the circumnuclear region, poorly studied in the literature. In §2 a description of the observations is given. The main characteristics of the nuclear and extended spectra are presented in §3 and §4, respectively. Photoionization model predictions for the most intense lines are discussed in §5, whereas the calculations of the central mass based on stellar features

appear in §6. Finally, our concluding remarks are presented in §7.

## 2 THE OBSERVATIONS

The spectra were obtained at the NASA 3m Infrared Telescope Facility (IRTF) in October 30, 2007. The SpeX spectrograph (Rayner et al., 2003) was used in the short cross-dispersed mode (SXD,  $0.8 - 2.4 \mu\text{m}$ ). The detector employed consisted of a  $1024 \times 1024$  ALADDIN 3 InSb array with a spatial scale of  $0.15''/\text{pixel}$ . A  $0.8'' \times 15''$  slit oriented in the north-south direction was used, providing a spectral resolution of  $360 \text{ km/s}$ . This value was determined both from the arc lamp and the sky line spectra and was found to be constant with wavelength along the observed spectra. During the observations the seeing was  $\sim 1.3''$ . Observations were done nodding in an object-sky-sky-object pattern with integration time of 180 s per frame and total on-source integration time of 12 minutes. After the galaxy, the A0V star HD18571 was observed as telluric standard and to flux calibrate the object. The spectral reduction, extraction and wavelength calibration procedures were performed using SPEXTOOL, the in-house software developed and provided by the SpeX team for the IRTF community (Cushing, Vacca & Rayner, 2004). The S/N of the spectra varies from  $\sim 43$  at the nuclear aperture to  $\sim 13$  at the most external apertures. Intermediate regions have S/N of  $\sim 20$ .

Figure 1 shows the position of the slit superimposed in the galaxy contours obtained from Galliano et al. (2003). From our data, we found that the light peak of the nuclear aperture in the K-band coincides in position with that determined by Galliano et al. (2003) for the same band. The gray contours show the 6 cm emission (Gallimore et al. 1996) and the red dotted contours show the  $20 \mu\text{m}$  image (Alloin et al. 2000). For NGC 1068, 17 extractions were made along the spatial direction: one, of radius  $0.8''$ , centered at the peak of the K-band distribution, and eight more, of  $0.2''$  in radius, at each side of it. In addition, in order to study in detail the variations of line profiles and continuum emission with distance, the nuclear aperture were subdivided into seven smaller apertures (called nuc\_a to nuc\_g in Figure 1) of  $0.2''$  of radius each. We are aware that these smaller apertures cannot be used for flux estimates because they are oversampled. The 1-D spectra were then corrected for telluric absorption and flux calibrated using Xtellcor (Vacca, Cushing & Rayner, 2003), another in-house software developed by the IRTF team. Finally, the different orders of the galaxy spectrum were merged to form a single 1-D frame. It was later corrected for redshift, determined from the average  $z$  measured from the most conspicuous lines. No Galactic extinction correction was applied because it is negligible at NIR ( $A_{\text{nir}}=0.112$ ).

## 3 NUCLEAR SPECTRA

Below we describe in detail the main features, both in emission and absorption, detected in the nuclear region of NGC 1068, which correspond to the spectrum covering  $1''.6$ , centered on the maximum of the galaxy profile. The resulting nuclear spectra in the ZJ, H and K ranges are plotted in

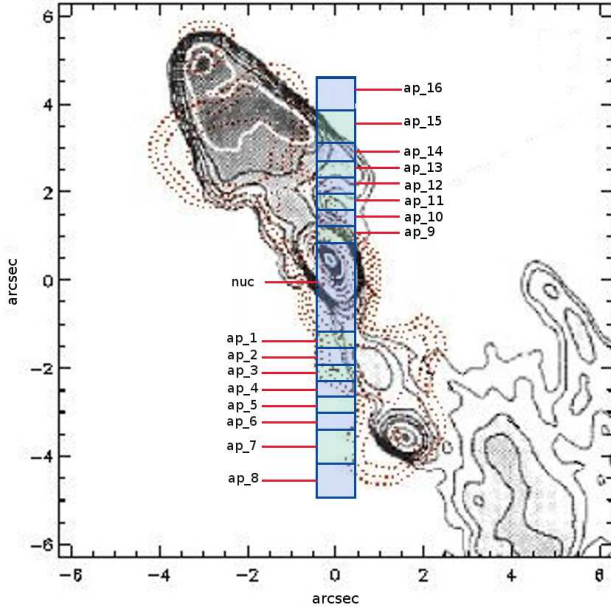


**Figure 1.** NGC 1068 contours obtained from Galliano et al. (2003) with the position of the IRTF slit superimposed. The gray contours show the 6 cm emission (Gallimore et al. 1996) and the red dotted contours show the 20  $\mu$ m image (Alloin et al. 2000)

Figures 2, 3 and 4, respectively, where the wavelengths have been translated to the observer's rest frame.

### 3.1 Emission lines

An inspection to Figures 2, 3 and 4 allows us to state that the most conspicuous features in the nuclear spectrum are [S III] $\lambda\lambda$ 0.907, 0.953  $\mu$ m, He I  $\lambda$ 1.083  $\mu$ m, Pa $\beta$ , [Fe II] $\lambda$ 1.643  $\mu$ m, Pa $\alpha$ , and the coronal lines [Si X] $\lambda$ 1.430  $\mu$ m, and [Si VI] $\lambda$ 1.962  $\mu$ m. Pa $\gamma$  and Br $\gamma$  are also present, but very weak. Pa $\gamma$  is in the wing of the very strong He I line. Pa $\alpha$  could not be measured because it partially falls in the gap between orders. Emission from H<sub>2</sub> molecule is clearly detected, whose most prominent lines are the transitions H<sub>2</sub> 1-0 (S2) and H<sub>2</sub> 1-0 (S1), although only H<sub>2</sub> 1-0 (S1) could be measured. H<sub>2</sub> 1-0 (S3) is not clear in the nuclear spectra because it is too close to the [Si VI] line, which is very broad. The flux of H<sub>2</sub> can be used to derive the mass of hot molecular gas, as shown in section 4.3.

Several other lines of lower intensity are detected in the ZJ spectra, namely [Ca I] $\lambda$ 0.985  $\mu$ m, [S VIII] $\lambda$ 0.991  $\mu$ m, He II  $\lambda$ 1.012  $\mu$ m, [S II] $\lambda$ 1.032  $\mu$ m (a blend of 4 [S II] transitions), [P II] $\lambda$ 1.188  $\mu$ m, [Fe II] $\lambda$ 1.257  $\mu$ m and the coronal line [Si X] $\lambda$ 1.252  $\mu$ m. Wherever possible, emission line fluxes for all features were measured assuming that the line profiles can be represented by a single or a sum of gaussian profiles. The continuum underneath each line was fit by a low-order polynomial, usually a straight line. The SMART routine (Higdon et al. 2004), a software developed by the Infrared Spectrograph (IRS) Instrument Team, originally designed to perform real-time processing and analysis of IRS data, was used for this purpose.

**Table 1.** Observed nuclear emission-line fluxes and EWs

Line	$\lambda$ ( $\mu$ m)	Flux ( $10^{-13}$ ergs cm $^{-2}$ s $^{-1}$ )	EW ( $\mu$ m)
[S III]	0.907	$7.50 \pm 0.77$	$0.0085 \pm 0.0008$
[S III]	0.953	$19.80 \pm 2.03$	$0.0242 \pm 0.0026$
[C I]	0.985	$0.91 \pm 0.11$	$0.0024 \pm 0.0003$
[S VIII]	0.991	$0.91 \pm 0.11$	$0.0015 \pm 0.0002$
He II	1.012	$1.61 \pm 0.17$	$0.0023 \pm 0.0006$
[S II]	1.032	$2.81 \pm 0.36$	$0.0035 \pm 0.0008$
He I	1.083	$17.00 \pm 1.76$	$0.0327 \pm 0.0071$
Pa $\gamma$	1.093	$0.97 \pm 0.12$	$0.0026 \pm 0.0004$
[P II]	1.188	$0.78 \pm 0.14$	$0.0010 \pm 0.0002$
[S IX]	1.252	$0.88 \pm 0.12$	$0.0021 \pm 0.0003$
[Fe II]	1.257	$0.91 \pm 0.13$	$0.0023 \pm 0.0012$
Pa $\beta$	1.282	$2.24 \pm 0.29$	$0.0033 \pm 0.0007$
[Si X]	1.430	$1.59 \pm 0.18$	$0.0021 \pm 0.0007$
[Fe II]	1.643	$0.72 \pm 0.09$	$0.0008 \pm 0.0002$
H <sub>2</sub> 1-0 S(3)	1.956	$0.54 \pm 0.07$	$0.0003 \pm 0.0001$
[Si VI]	1.962	$3.39 \pm 0.37$	$0.0030 \pm 0.0009$
H <sub>2</sub> 1-0 S(1)	2.121	$0.35 \pm 0.05$	$0.0002 \pm 0.0001$
Br $\gamma$	2.165	$0.42 \pm 0.06$	$0.0002 \pm 0.0001$
[Ca VIII]	2.322	$1.01 \pm 0.23$	$0.0005 \pm 0.0002$

The results are shown in Table 1. Errors on the fluxes were obtained from the values given by SMART, which is calculated based on the residual of the fit and the flux calibration error, which is about 10 % for the infrared.

The detection of [P II] with considerable strength is particularly interesting. As explained by Mazzalay & Rodríguez-Ardila (2007), in the Sun this element is a factor  $\sim 1000$  times less abundant than carbon. In the nuclear spectrum of NGC 1068 we find a ratio of [P II]/[C I] equal to 0.8. If the P/C abundance is about solar, the [P II] line should not be present, unless carbon, like iron, might be locked in grains. This indicates that phosphorus may be overabundant by a factor of 10-20 compared to its solar abundance, relative to hydrogen.

The observed line widths are between 800 - 1000 km s $^{-1}$ . This is in agreement with what is found in the optical region (Pelat & Alloin 1980). Although NGC 1068 has been considered a prototypical Seyfert 2 galaxy, its forbidden lines are much wider than those of typical Seyfert 2s. Moreover, some emission-line profiles show multiple components (Pelat & Alloin 1980, Alloin et al. 1983, Meaburn & Pedlar 1986) also seen in the NIR as we show in section 4.1.

### 3.2 Absorption features

Several absorption features are clearly seen in the H- and K-band nuclear spectrum (Figures 3 and 4). In particular, we observe the following ones: Mg I 1.50  $\mu$ m, CO 1.58  $\mu$ m, Si I 1.59  $\mu$ m, CO 1.62  $\mu$ m, Mg I 1.71  $\mu$ m, CO 2.29  $\mu$ m, CO 2.35  $\mu$ m and CO 2.38  $\mu$ m. These features are identified after their main contributor, although, depending on the dominant stellar type, other features may become dominant.

The CO 1.62  $\mu$ m can be used to obtain a rough estimate of the contribution of the stellar population flux to the H band. This is done by measuring the depth of the  $^{12}\text{CO}(6-3)$  overtone bandhead at 1.62  $\mu$ m. We found that the observed depth is  $12\% \pm 1\%$  of the continuum. This can be compared to the  $\sim 20\%$  that is typically expected for a

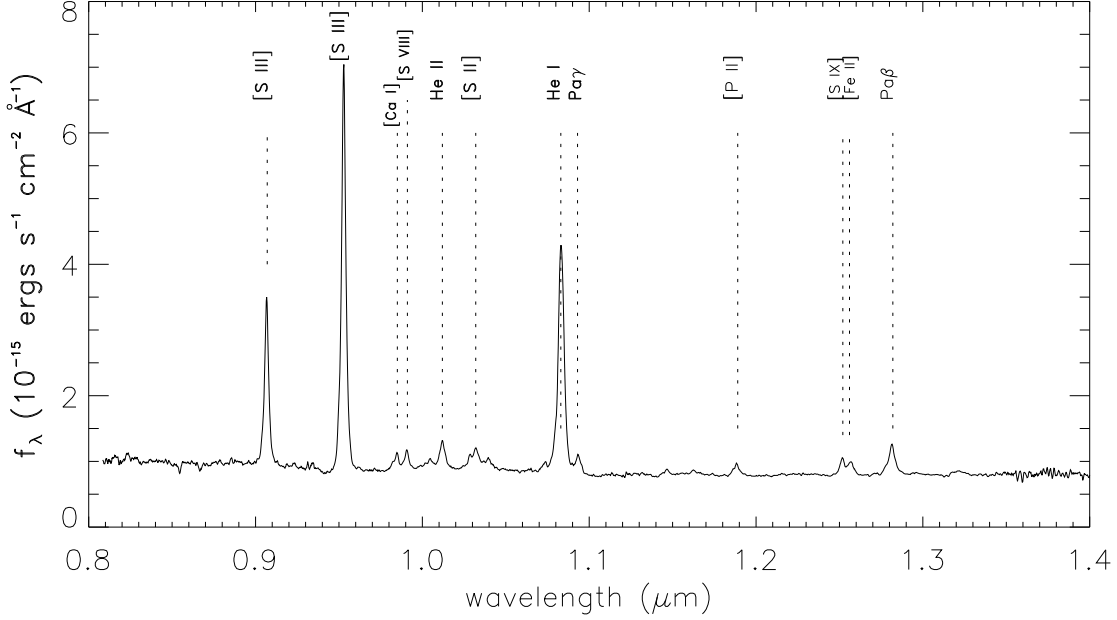


**Figure 2.** Flux calibrated spectrum in the ZJ range of the nuclear region of NGC 1068. The aperture width is  $1''.6$ . Major emission lines detected are identified.

population of GKM supergiants that dominates the H band light for a stellar population older than  $10^7$  yr (Schinnerer et al. 1998). It can thus be roughly estimated that about  $60\% \pm 5\%$  of the total flux in the H band continuum is due to GKM supergiants. Following Schinnerer et al. (1998), although these stars dominate the stellar emission in the H band, about one-third of the total stellar flux comes from stars of other stellar classes. Therefore,  $90\% \pm 8\%$  of the nuclear H band continuum could be of stellar origin. This is in reasonable agreement with the  $74\% \pm 8\%$  determined by Cid Fernandes et al. (2001) for this object, based on optical spectroscopy. This means that the H-band continuum is essentially dominated by the stellar population, with only  $\sim 10 - 20\%$  due to the AGN. This calculations show how the NIR spectroscopy is a potential tool to unveil hidden starburst components, either in highly obscured objects or in those in which the optical continuum emission is dominated by the AGN component (as in Seyfert 1 galaxies).

One way of estimating the age of the stellar population in the NIR is using the CO index defined by Ivanov et al. (2000), for the absorption feature starting at  $2.29 \mu\text{m}$ . This index is supposed to be insensitive to extinction and to possible uncertainties in the continuum shape of the infrared spectra and it is defined as

$$CO = -2.5 \log \left( \frac{\langle F_{2.295} \rangle}{\langle F_{2.282} \rangle} \right) \quad (1)$$

where  $\langle F_{2.282} \rangle$  and  $\langle F_{2.295} \rangle$  are the average fluxes within a bandwidth of  $0.01 \mu\text{m}$ , centered on the blue continuum and on the bandhead respectively. For the nuclear aperture we obtained an index of  $-0.01 \pm 0.05$ . This value is extremely low for a Seyfert 2 galaxy, according to the sample of Ivanov et al. Notice that in a Seyfert galaxy nucleus, the late-

type stellar features are substantially diluted by non-stellar nuclear emission. NGC 1068 is probably an extreme case, since its nuclear spectrum shows a very steep increase in the K band continuum flux with wavelength (Figure 4), much steeper than what is expected for a non-thermal power-law source. The K band excess of emission is probably due to thermal radiation from hot dust (Thatte et al. 1997).

In order to minimize the influence of the shape of the continuum, we normalized the spectrum in this region using a linear fit in the region between  $2.20$  and  $2.26 \mu\text{m}$ , where there are no apparent features. After dividing the spectrum by this fit the CO index is recalculated. The new value is  $0.01 \pm 0.05$ . Thus, the low value is not caused by the shape of the spectrum and suggests that there is no evidence for a strong starburst, in agreement with the results of Ivanov et al. (2000) for Seyfert galaxies, but contrary to what was found in the H band.

Nevertheless, it is really hard to estimate the true dilution of the bandhead by the continuum. The best way would be to do a full stellar population fitting, including a non-stellar component. This is out of the scope of this paper, but is presented in detail in a follow-up paper (Martins et al. 2010).

#### 4 SPECTRA OF THE EXTENDED REGION

In addition to the nuclear spectra discussed in the preceding section, the spatial information contained in the slit allowed us to extract the spectra corresponding to the narrow line region and to the extended line region of NGC 1068 to the limits of  $\sim 350$  pc north and south of the nucleus. Gas kin-

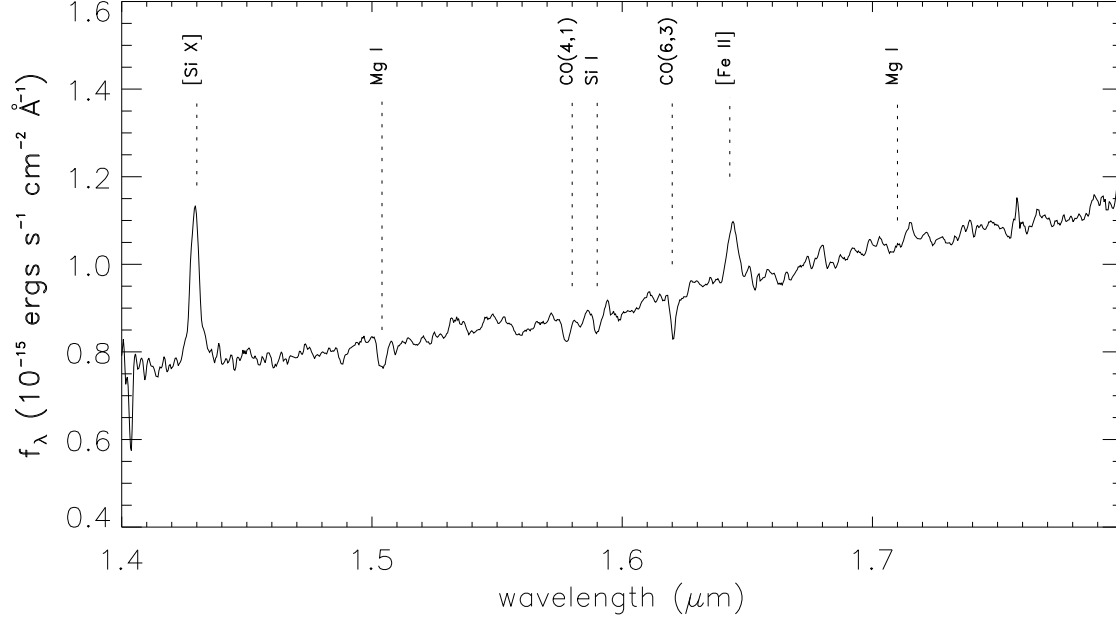


**Figure 3.** Same as Figure 2, but in the H band.

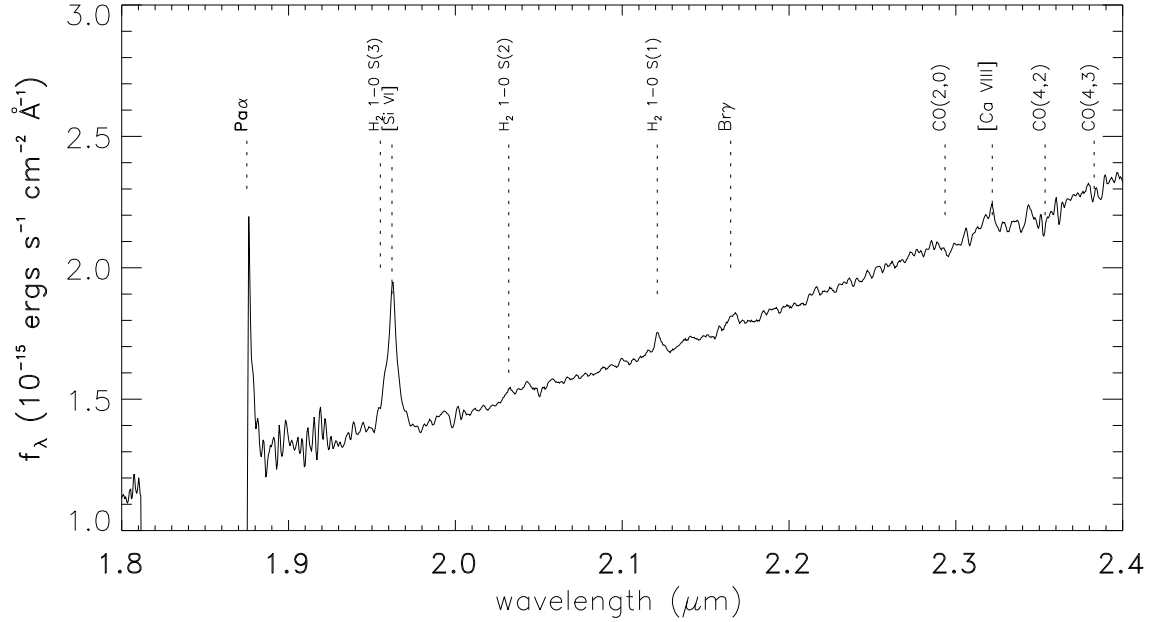


**Figure 4.** Same as Figure 2, but in the K band. Note that Pa $\alpha$  is severely affected by telluric absorption.

matics as well as extinction and the molecular and [Fe II] lines will be studied in more detail in the following sections.

#### 4.1 Gas kinematics

The spectra for all integrated apertures are presented in Figures 5-7, where the wavelengths are in the observer's rest frame. It is easy to see that the most conspicuous lines show a double peaked profile. One component is in the rest frame

of the galaxy (primary component, hereafter) while the other (second component, hereafter) is either blueshifted towards the north of the nucleus or redshifted to the south. The relative intensity of the peaks also varies with distance, as shown in Figure 8 for  $[\text{S III}]\lambda 0.953\text{ }\mu\text{m}$ , the strongest line in our spectra. It can be seen that  $[\text{S III}]$  is detected at distances of up to  $\sim 350$  pc from the nucleus. As explained in Sec. 2, for the purpose of comparing the line profiles we divided the nuclear spectra ( $1.6''$  aperture) into seven smaller apertures (see Fig. 1). The aperture named “nuc\_a”, centered on the peak of the continuum light distribution, is extracted over the central  $0.4''$  window and the remaining six with apertures  $0.2''$  wide. Although the integrated flux of these smaller apertures are oversampled because the extraction window is smaller than the seeing value, this approach allows us to study line profiles, which clearly show changes along the spatial direction at scales down to 20 pc.

A comparison of the line profiles in velocity space observed in the most conspicuous emission lines is presented in Figure 9. In this figure, the continuum underneath each line was adjusted using a linear interpolation and then subtracted. It can be seen that the coronal line  $[\text{S VIII}]$  shows a profile very similar to that of  $[\text{S III}]$ , and second components can be clearly seen. The molecular  $\text{H}_2$  lines also show scarce evidence of a second component, not so clear since the line is weak. They are also narrower than the emission features of other species outside the nucleus, which indicates that it might be formed in a different region. Indeed, NIR observations has shown that the  $\text{H}_2$  emission is distributed mainly along a direction perpendicular to the ionizing cone (Galliano & Alloin 2002). The  $[\text{Fe II}]$  lines seem to follow the  $\text{H}_2$  lines more closely.

We did not identify a broad component with FWHM  $\sim 2000\text{ km s}^{-1}$  in any line, although they have been reported on FUSE observations (Zheng et al. 2008). That may be because FUSE slit collects emission from a block of regions spanning several arcseconds perpendicular to the conical axis and the total line emission from these regions may be blended into one broad component. Since we are observing much smaller regions with each aperture, we minimize this effect.

Not all emission lines have double peaked profiles. This is the case of high ionization lines such as  $[\text{S VIII}]$  and  $[\text{Si X}]$  as well as molecular lines of  $\text{H}_2$ . Moreover, low ionization lines like  $[\text{Ca I}]$  or  $[\text{P II}]$  also seem to be devoided of a double-peak structure but these are faint lines. The lack of splitting may be either by intrinsic reasons or due to low S/N. In Figure 10, the relative flux of the most conspicuous emission lines are shown as a function of the distance to the center. The fluxes were normalized relative to the nucleus to allow the comparison between the different lines. Negative distances represent the northern direction and positive distances the southern one. For double peaked lines, the upper panel shows the distribution of the primary component while the bottom panel that of the secondary component. It can be seen that the second component of  $[\text{S III}]\lambda 0.953\text{ }\mu\text{m}$  and  $\text{He I } 1.083\text{ }\mu\text{m}$  are observed up to 200 pc from the nucleus. Indeed, it seems that there is a maximum of the second components between 100 - 150 pc from the center. As for the primary components, evidence of emission up to 300 pc from the center is observed although it becomes too much faint to be mea-

sured at  $3\sigma$  level. Note that the  $[\text{Fe II}]$  emission is the most extended of all lines analyzed.

The flux gas distribution shown in Figure 10 and mapped by the first time in the literature with data in the interval  $0.8\text{--}2.4\text{ }\mu\text{m}$  confirms previous reports in the optical and MIR in the sense that the northern zone has stronger emission than the southern one (Mazzalay et al. 2009; Geballe et al. 2009). This can be attributed to the strong extinction towards the observer. In this scenario, the ionization cone is partially hidden from our view because it crosses the host galaxy plane. Note also that high ionization lines like  $[\text{Si X}] \lambda 1.430\text{ }\mu\text{m}$  and  $[\text{Si VI}] \lambda 1.954\text{ }\mu\text{m}$  are detected only up to  $\sim 200$  pc from the nucleus. This is a clear indication that the gas is more ionized near the nucleus.

The observed emission features of the extended region were also measured with the software SMART. The results are shown in Tables 2 and 3. Errors were estimated the same way as in Table 1.

## 4.2 Extinction

The extinction towards the nucleus and circumnuclear region was determined from the comparison of the predicted and observed emission line ratios assuming the standard extinction law of Cardelli et al. (1989) for  $R_V = 3.1$ . From our observed lines, two line ratios are extinction indicators:  $\text{Pa}\beta/\text{Pa}\gamma$  and  $[\text{Fe II}] \lambda 1.257\text{ }\mu\text{m}/\lambda 1.643\text{ }\mu\text{m}$ . We added both components of  $\text{Pa}\beta$  for this purpose. The reason for this is that  $\text{Pa}\gamma$  has no second components, probably because it is a weak line and it was not possible to distinguish them. When using only the primary component of  $\text{Pa}\beta$ , many ratios give unphysical results.  $\text{Pa}\alpha$  could not be used in this calculation because it was severely affected by telluric transmission. Moreover,  $\text{Br}\gamma$  was only detected in the central aperture.

For hydrogen we used the intrinsic ratios for the case B given by Osterbrock (1989). The pair of  $[\text{Fe II}]$  lines used to estimate the extinction share the same upper level, meaning that the intensity ratio depends only on the energy differences between the lines and their Einstein-A coefficients, making this line ratio a useful probe of reddening. The intrinsic value of the  $[\text{Fe II}] \lambda 1.257\text{ }\mu\text{m}/\lambda 1.643\text{ }\mu\text{m}$  ratio was taken from Bautista & Pradhan (1998), calculated from Nussbaumer & Storey (1988) transition probabilities. Table 4 shows the values of extinction found for each aperture. For the errors in this table we only considered the errors in the line measurements and not in the flux calibration.

The results point to extinction variations up to a factor of 4 within the NLR. However, the  $E(B-V)$  derived from the hydrogen ratios suffer from two major problems: the  $\text{Pa}\beta$  line may be contaminated with the  $[\text{Fe II}] \lambda 1.278\text{ }\mu\text{m}$ , leading to an overestimation of the reddening determined from  $\text{Pa}\beta/\text{Pa}\gamma$ . Also, the  $\text{Pa}\gamma$  line is in the wing of the much stronger  $\text{He I } 1.083\text{ }\mu\text{m}$  line. Therefore, problems with the deblending of these two lines could lead to larger uncertainties in this calculation. Note that the uncertainties quoted are determined only from the S/N around the region containing the lines of interest and they do not take into account potential deblending issues.

Differences between the reddening obtained from the  $[\text{Fe II}]$  lines and hydrogen lines are expected, since these lines are probably not emitted from the same region. Keep in

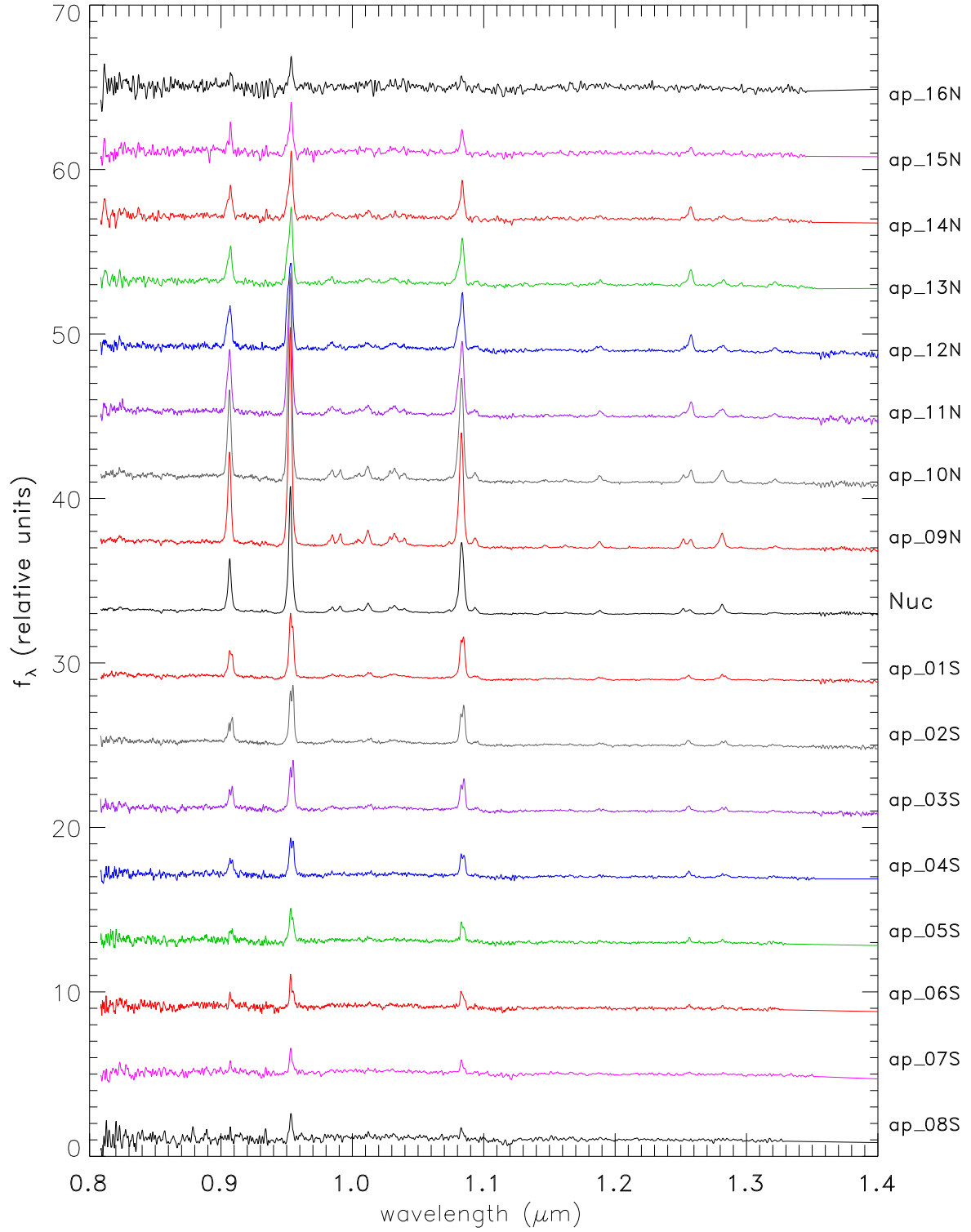


**Figure 5.** Spectra of all apertures of NGC 1068 in the ZJ range. From the top to the bottom the spectra correspond to the apertures from north to south.

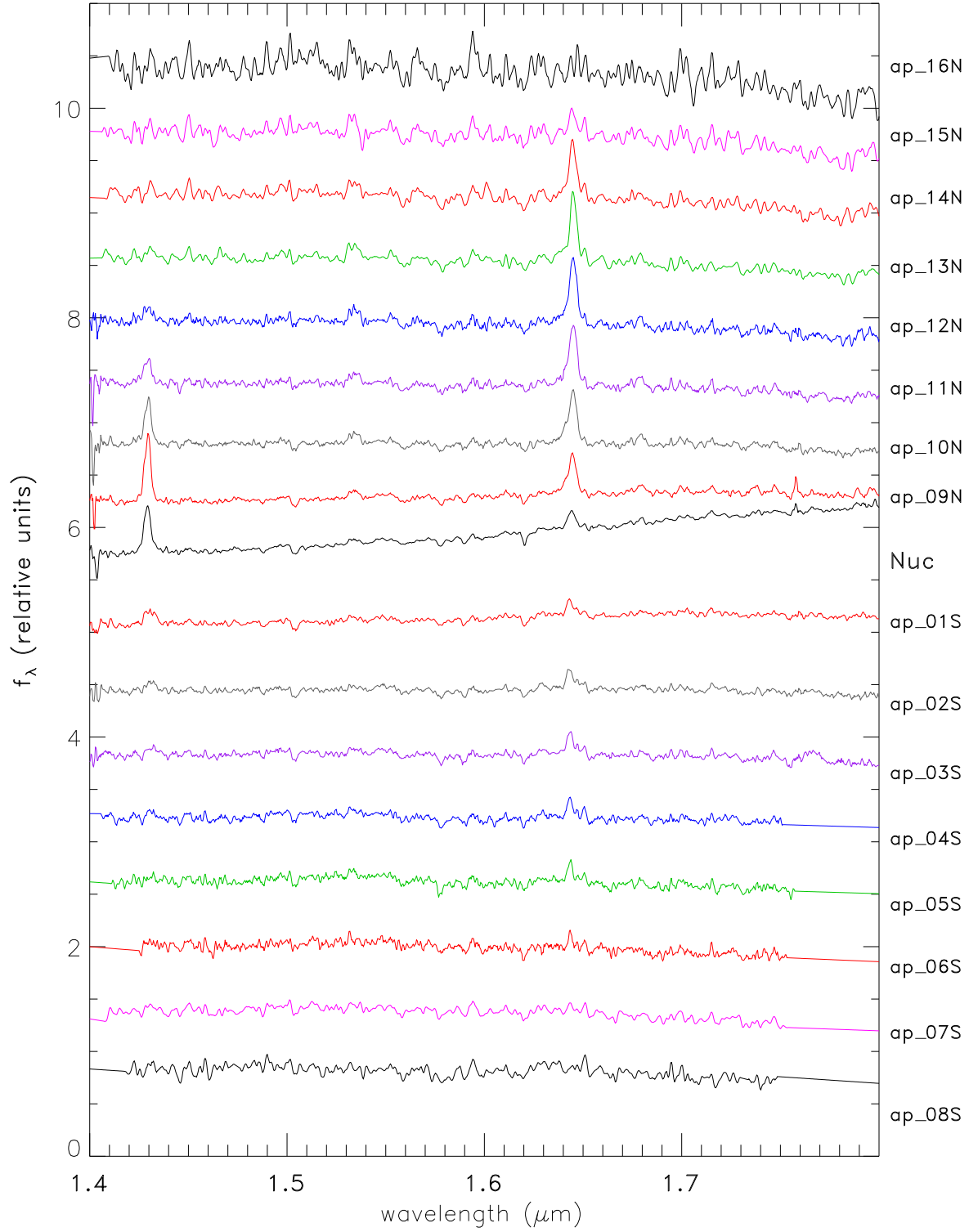


**Figure 6.** Same as in Figure 5, but in the H band.



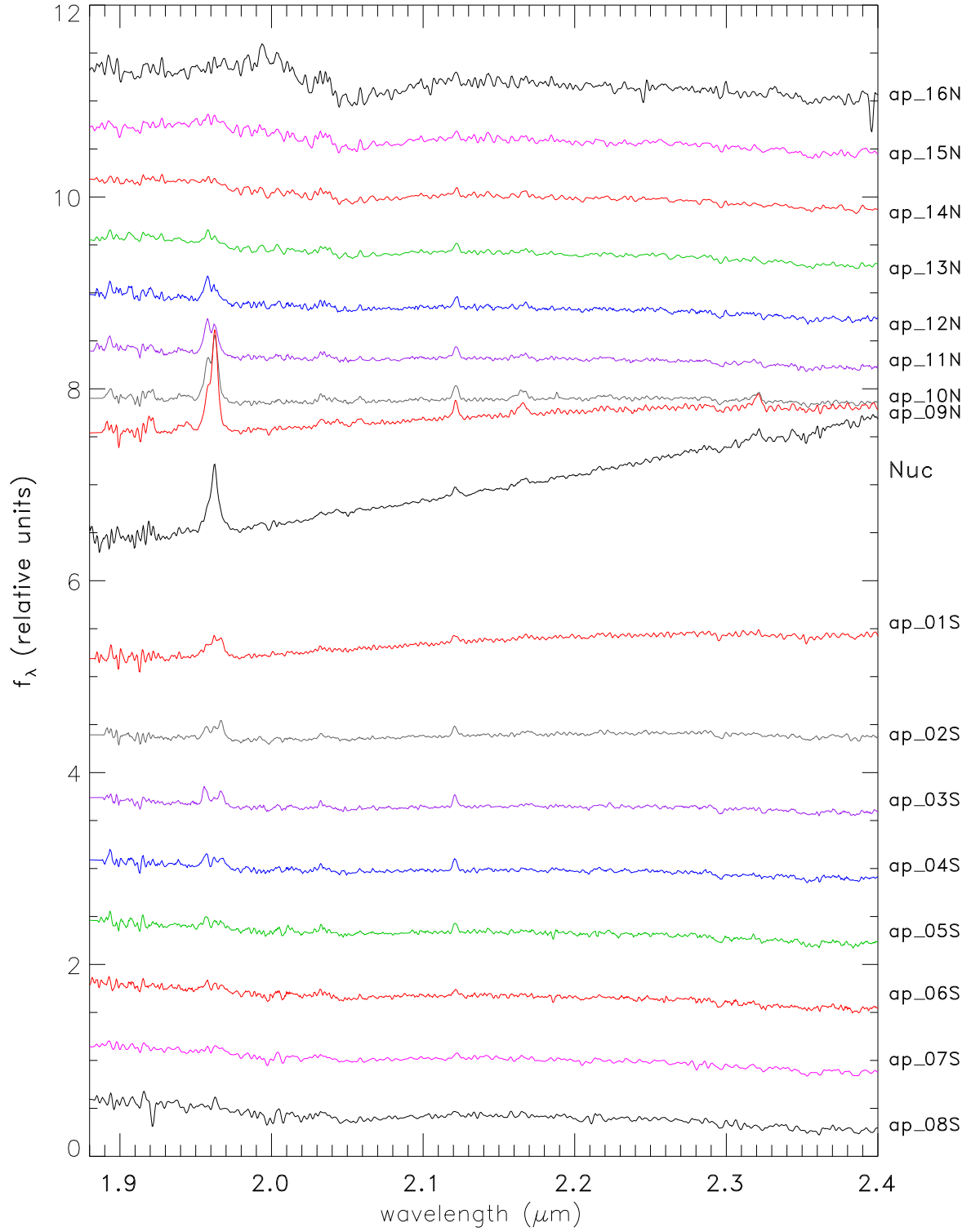


**Figure 7.** Same as in Figure 5 but in the K band.

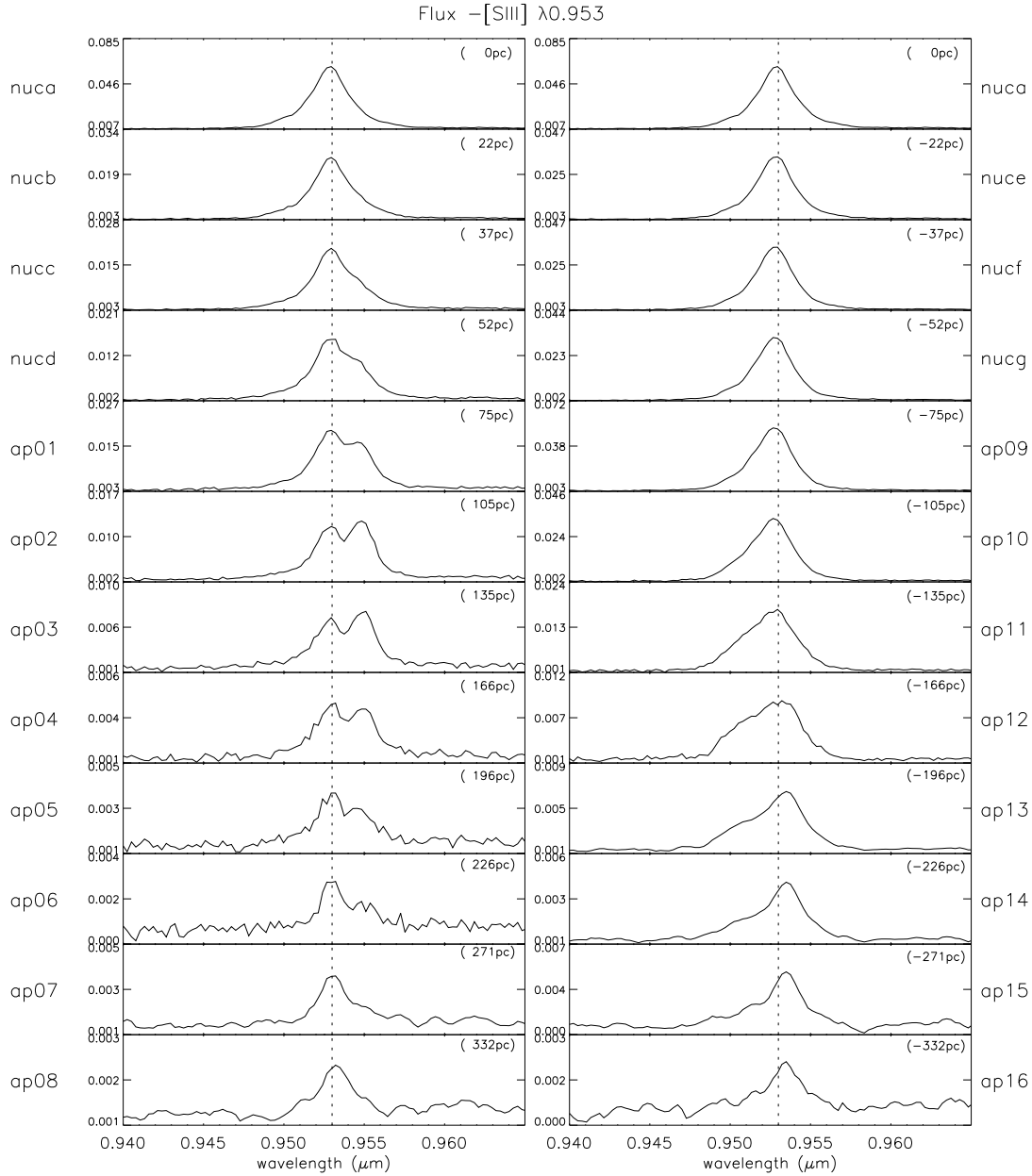


**Figure 8.** Profile of the [SIII] $\lambda 0.953$   $\mu\text{m}$  for all apertures. Left panels show the apertures to the south, where the second peak is redshifted. Right panels are the apertures to the north, where the second peak is blueshifted. The first plot in each column is the very central aperture, plotted in both columns for comparison.

mind that the uncertainties in the  $E(B-V)$  from the [Fe II] lines can also be large since these lines are intrinsically weak.

The analysis of Kraemer et al. (1998) indicates that there may be some dust mixed with gas in various amounts in this galaxy. Veilleux et al. (1997) obtained a value of  $E(B-V) = 0.34$  using the Balmer decrement. Our average result for the NLR from both determinations is above this value. This might be an indication that the NIR might come from dustier, deeper regions of the NLR.

The extinction obtained from the two line ratios for the various apertures are shown in Figure 11. The nuclear region seems to be more dusty than the adjacent regions but secondary peaks of extinction are also observed, with

maximums around 150 - 200 pc from each side of the nucleus. These positions are also close to the region where the second component of the emission lines has a maximum, and may be associated to the presence of dense clouds mixed with dust in this region.

### 4.3 $\text{H}_2$ and [Fe II] lines

Emission from  $\text{H}_2$  molecules are observed in most apertures of NGC 1068, and has been the subject of extensive analysis by different authors. Reunanen et al. (2003) suggest a star formation origin for these lines as a result of UV heating from OB stars. Whether the heating mechanism is

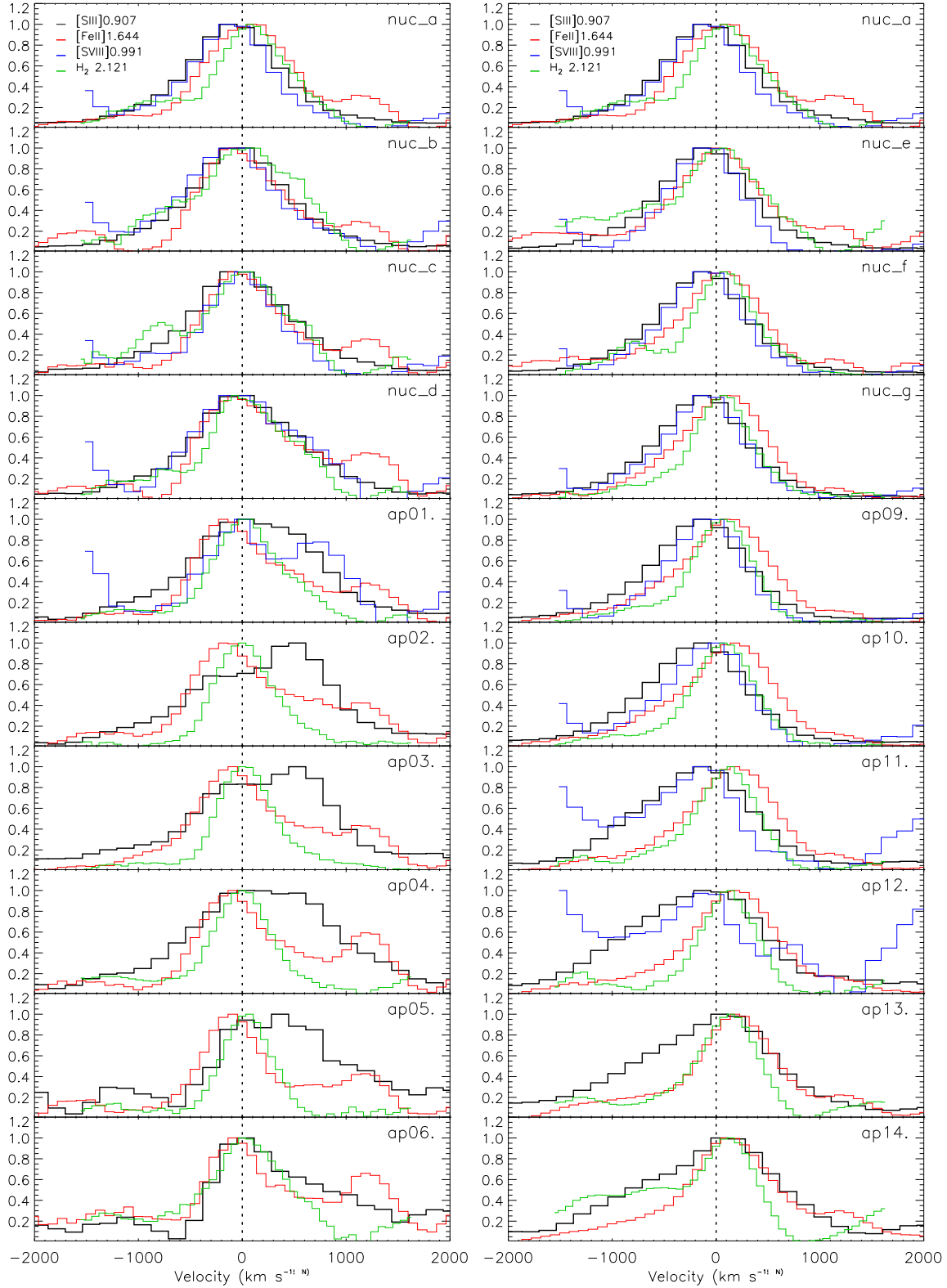


**Figure 9.** Profile of emission lines in the velocity space. Left panels show the apertures to the south, where the second peak is redshifted. Right panels show the apertures to the north, where the second peak is blueshifted. The first plot in each column is the very central aperture, plotted in both columns for comparison. Lines were only plotted for the apertures where they have measurable fluxes.

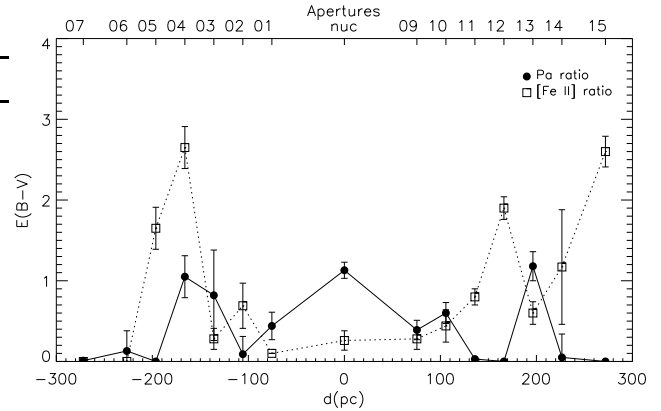
**Table 2.** Observed emission-line fluxes of all South non-nuclear apertures

South - Main components									
Flux ( $10^{-14}$ ergs cm $^{-2}$ s $^{-1}$ )									
Line	$\lambda$ ( $\mu$ m)	Ap01	Ap02	Ap03	Ap04	Ap05	Ap06	Ap07	Ap08
[S III]	0.907	$5.81 \pm 1.10$	$1.63 \pm 0.27$	$1.28 \pm 0.25$	$1.31 \pm 0.22$	$1.04 \pm 0.19$	$0.45 \pm 0.08$	$0.61 \pm 0.06$	$0.23 \pm 0.03$
[S III]	0.953	$14.21 \pm 1.80$	$6.66 \pm 0.85$	$3.95 \pm 0.71$	$3.93 \pm 0.70$	$1.84 \pm 0.33$	$0.96 \pm 0.14$	$1.90 \pm 0.24$	$1.22 \pm 0.15$
[C I]	0.985	$1.60 \pm 0.26$	$0.48 \pm 0.09$	$0.45 \pm 0.11$	$0.64 \pm 0.13$	-	-	-	-
[S VIII]	0.991	$0.21 \pm 0.07$	-	-	-	-	-	-	-
He II	1.012	$1.12 \pm 0.37$	$1.00 \pm 0.15$	$0.63 \pm 0.16$	$0.61 \pm 0.12$	$0.34 \pm 0.10$	-	$0.11 \pm 0.02$	$0.22 \pm 0.03$
[S II]	1.032	$3.50 \pm 0.77$	$1.28 \pm 0.28$	$0.81 \pm 0.16$	-	-	-	$0.19 \pm 0.03$	-
He I	1.083	$11.48 \pm 1.56$	$3.64 \pm 0.48$	$2.36 \pm 0.32$	$2.38 \pm 0.43$	$1.43 \pm 0.34$	$0.77 \pm 0.11$	$0.84 \pm 0.12$	$0.58 \pm 0.08$
Pa $\gamma$	1.093	$1.13 \pm 0.19$	$0.74 \pm 1.45$	$0.58 \pm 0.13$	$0.62 \pm 0.14$	-	$0.07 \pm 0.01$	$0.08 \pm 0.01$	-
[PII]	1.188	$1.10 \pm 0.19$	$0.82 \pm 0.12$	$0.64 \pm 0.10$	$1.01 \pm 0.13$	-	-	-	-
[S IX]	1.252	$0.39 \pm 0.08$	$0.11 \pm 0.02$	$0.72 \pm 0.10$	$0.22 \pm 0.09$	-	-	-	-
[Fe II]	1.257	$1.39 \pm 0.28$	$1.06 \pm 0.15$	-	$0.37 \pm 0.08$	$0.28 \pm 0.07$	$0.22 \pm 0.05$	$0.36 \pm 0.05$	-
Pa $\beta$	1.282	$2.22 \pm 0.41$	$1.04 \pm 0.14$	$1.06 \pm 0.15$	$0.65 \pm 0.12$	$0.39 \pm 0.09$	$0.13 \pm 0.03$	$0.12 \pm 0.02$	-
[Si X]	1.430	$1.43 \pm 0.27$	$1.25 \pm 1.05$	-	-	-	-	-	-
[Fe II]	1.643	$0.76 \pm 0.59$	$1.27 \pm 0.17$	$0.57 \pm 0.07$	$0.58 \pm 0.08$	$0.33 \pm 0.06$	$0.15 \pm 0.03$	-	-
[Si VI]	1.962	$3.28 \pm 0.41$	$1.06 \pm 0.17$	$0.17 \pm 0.03$	$0.16 \pm 0.03$	-	-	$0.23 \pm 0.04$	$0.12 \pm 0.01$
H <sub>2</sub> 1-0 S(1)	2.121	$0.65 \pm 0.13$	$0.32 \pm 0.04$	$0.24 \pm 0.03$	$0.25 \pm 0.03$	$0.14 \pm 0.02$	$0.10 \pm 0.02$	$0.12 \pm 0.02$	$0.10 \pm 0.01$
Br $\gamma$	2.165	-	-	-	-	-	-	-	-
[Ca VIII]	2.322	$0.21 \pm 0.03$	-	-	-	-	-	-	-
South - Second components									
Flux ( $10^{-14}$ ergs cm $^{-2}$ s $^{-1}$ )									
Line	$\lambda$ ( $\mu$ m)	Ap01	Ap02	Ap03	Ap04	Ap05	Ap06	Ap07	Ap08
[S III]	0.907	$2.13 \pm 0.44$	$2.77 \pm 0.52$	$1.25 \pm 0.13$	$1.24 \pm 0.24$	-	-	-	-
[S III]	0.953	$4.16 \pm 0.81$	$4.81 \pm 0.87$	$2.87 \pm 0.31$	$2.87 \pm 0.54$	$0.76 \pm 0.16$	$0.65 \pm 0.14$	-	-
He II	1.012	$0.17 \pm 0.31$	-	-	-	-	-	-	-
He I	1.083	$4.09 \pm 0.79$	$4.46 \pm 0.82$	$2.20 \pm 0.56$	$2.18 \pm 0.43$	$0.69 \pm 0.14$	$0.29 \pm 0.07$	$0.25 \pm 0.07$	-
Pa $\beta$	1.282	$0.20 \pm 0.04$	$0.29 \pm 0.06$	$0.18 \pm 0.09$	$0.76 \pm 0.16$	-	-	-	-
[Si VI]	1.962	-	$0.76 \pm 0.14$	$0.35 \pm 0.11$	$0.39 \pm 0.09$	-	-	-	-

**Table 4.** Flux ratios and E(B-V)

Line	Pa $\beta$ /Pa $\gamma$	E(B-V)	[FeII]1.257/1.643	E(B-V)
Ap07	$1.49 \pm 0.31$	$< 0.01$	-	-
Ap06	$1.84 \pm 0.48$	$0.13 \pm 0.25$	$1.54 \pm 0.49$	$< 0.92$
Ap05	-	-	$0.85 \pm 0.22$	$1.65 \pm 0.26$
Ap04	$2.27 \pm 0.55$	$1.05 \pm 0.26$	$0.64 \pm 0.17$	$2.65 \pm 0.26$
Ap03	$1.31 \pm 0.55$	$0.82 \pm 0.56$	$1.26 \pm 0.16$	$0.28 \pm 0.13$
Ap02	$1.83 \pm 0.41$	$0.09 \pm 0.22$	$1.12 \pm 0.31$	$0.69 \pm 0.28$
Ap01	$1.98 \pm 0.51$	$0.44 \pm 0.17$	$1.83 \pm 0.51$	$< 0.10$
Nuc	$2.31 \pm 0.24$	$1.13 \pm 0.10$	$1.26 \pm 0.15$	$0.26 \pm 0.12$
Ap09	$1.96 \pm 0.32$	$0.39 \pm 0.12$	$1.26 \pm 0.16$	$0.28 \pm 0.13$
Ap10	$2.05 \pm 0.34$	$0.60 \pm 0.13$	$1.20 \pm 0.23$	$0.44 \pm 0.20$
Ap11	$1.50 \pm 0.38$	$< 0.03$	$1.09 \pm 0.10$	$0.80 \pm 0.10$
Ap12	$1.17 \pm 0.35$	-	$0.80 \pm 0.11$	$1.90 \pm 0.14$
Ap13	$2.33 \pm 0.49$	$1.18 \pm 0.18$	$1.15 \pm 0.16$	$0.60 \pm 0.14$
Ap14	$1.11 \pm 0.55$	$< 0.05$	$0.98 \pm 0.26$	$1.17 \pm 0.71$
Ap15	-	-	$0.65 \pm 0.12$	$2.60 \pm 0.19$

thermal or fluorescence is not clear because neither the 2-1 S(1) 2.247 $\mu$ m nor the 1-0 S(0) 2.223 $\mu$ m emission were detected in the nucleus. They derived an upper limit of 5300 K for the vibrational temperature in the inner few hundred of parsecs of this object.

**Figure 11.** E(B-V) derived from emission lines as a function of distance from the center. Negative distances represent the north direction and positive distances the south.

We used their method to estimate the mass of the hot molecular gas present in each aperture. Assuming  $T = 2000\text{K}$ , a transition probability  $A_S(1) = 3.47 \times 10^{-7} \text{ s}^{-1}$  (Turner et al. 1977) and the population fraction in the  $\nu =$

**Table 3.** Observed emission-line fluxes of all North non-nuclear apertures

North - Main components									
Flux ( $10^{-14}$ ergs cm $^{-2}$ s $^{-1}$ )									
Line	$\lambda(\mu\text{m})$	Ap09	Ap10	Ap11	Ap12	Ap13	Ap14	Ap15	Ap16
[S III]	0.907	$17.96 \pm 2.06$	$11.73 \pm 1.18$	$6.50 \pm 0.96$	$2.53 \pm 0.33$	$1.74 \pm 0.24$	$1.43 \pm 0.19$	$1.32 \pm 0.18$	$0.56 \pm 0.09$
[S III]	0.953	$46.14 \pm 6.96$	$30.03 \pm 3.01$	$16.33 \pm 2.10$	$7.46 \pm 0.99$	$4.83 \pm 0.62$	$2.94 \pm 0.39$	$3.25 \pm 0.45$	$1.24 \pm 0.15$
[C I]	0.985	$2.38 \pm 0.42$	$1.85 \pm 0.27$	$1.39 \pm 0.20$	$0.88 \pm 0.13$	$0.53 \pm 0.08$	$0.55 \pm 0.07$	-	-
[S VIII]	0.991	$1.86 \pm 0.30$	$1.40 \pm 0.21$	$0.67 \pm 0.10$	$0.21 \pm 0.04$	-	-	-	-
He II	1.012	$4.25 \pm 0.70$	$2.19 \pm 0.30$	$1.09 \pm 0.16$	$0.68 \pm 0.10$	$0.50 \pm 0.08$	$0.57 \pm 0.08$	-	-
[S II]	1.032	$6.36 \pm 1.05$	$4.15 \pm 0.57$	$2.30 \pm 0.30$	$0.90 \pm 0.12$	$0.69 \pm 0.09$	$0.30 \pm 0.05$	-	-
He I	1.083	$29.19 \pm 4.34$	$17.39 \pm 1.75$	$9.87 \pm 1.33$	$4.75 \pm 0.65$	$2.31 \pm 0.30$	$2.19 \pm 0.30$	$1.98 \pm 0.22$	$0.74 \pm 0.13$
Pa $\gamma$	1.093	$2.46 \pm 0.31$	$1.45 \pm 0.20$	$1.10 \pm 0.19$	$0.72 \pm 0.13$	$0.30 \pm 0.05$	$0.38 \pm 0.05$	-	-
[PII]	1.188	$2.01 \pm 0.22$	$1.46 \pm 0.19$	$1.01 \pm 0.13$	$1.01 \pm 0.13$	$0.39 \pm 0.06$	-	-	-
[S IX]	1.252	$2.31 \pm 0.28$	$1.68 \pm 0.23$	$0.81 \pm 0.12$	$0.99 \pm 0.16$	$0.36 \pm 0.06$	$0.22 \pm 0.04$	$0.15 \pm 0.03$	-
[Fe II]	1.257	$2.40 \pm 0.29$	$2.06 \pm 0.28$	$1.95 \pm 0.27$	$1.14 \pm 0.19$	$1.15 \pm 0.17$	$0.77 \pm 0.10$	$0.51 \pm 0.07$	-
Pa $\beta$	1.282	$4.81 \pm 0.70$	$2.44 \pm 0.32$	$1.02 \pm 0.42$	$0.85 \pm 0.12$	$0.52 \pm 0.08$	$0.27 \pm 0.04$	$0.24 \pm 0.04$	-
[Si X]	1.430	$2.41 \pm 0.30$	$1.06 \pm 0.15$	$0.76 \pm 0.11$	$0.45 \pm 0.09$	-	-	-	-
[Fe II]	1.643	$1.91 \pm 0.26$	$1.71 \pm 0.25$	$1.80 \pm 0.21$	$1.43 \pm 0.16$	$1.00 \pm 0.12$	$0.79 \pm 0.09$	$0.78 \pm 0.10$	-
[Si VI]	1.962	$5.51 \pm 0.69$	$2.42 \pm 0.36$	$0.86 \pm 0.12$	$0.43 \pm 0.10$	$0.13 \pm 0.03$	-	-	-
H <sub>2</sub> 1-0 S(1)	2.121	$0.76 \pm 0.10$	$0.53 \pm 0.06$	$0.32 \pm 0.04$	$0.21 \pm 0.04$	$0.13 \pm 0.02$	$0.08 \pm 0.01$	$0.15 \pm 0.03$	-
Br $\gamma$	2.165	$0.99 \pm 0.12$	$0.58 \pm 0.09$	-	$0.16 \pm 0.04$	-	$0.12 \pm 0.01$	-	-
[Ca VIII]	2.322	$1.14 \pm 0.17$	$0.39 \pm 0.09$	-	-	-	-	-	-

North - Second components									
Flux ( $10^{-14}$ ergs cm $^{-2}$ s $^{-1}$ )									
Line	$\lambda(\mu\text{m})$	Ap09	Ap10	Ap11	Ap12	Ap13	Ap14	Ap15	Ap16
[S III]	0.907	$2.49 \pm 0.33$	$1.66 \pm 0.22$	$1.20 \pm 0.16$	$2.29 \pm 0.33$	$1.18 \pm 0.18$	$0.55 \pm 0.08$	$0.43 \pm 0.07$	-
[S III]	0.953	$5.01 \pm 0.70$	$3.90 \pm 0.52$	$3.07 \pm 0.45$	$3.33 \pm 0.44$	$1.89 \pm 0.28$	$1.20 \pm 0.18$	$0.88 \pm 0.13$	-
[S VIII]	0.991	$0.47 \pm 0.07$	-	-	-	-	-	-	-
He II	1.012	-	-	-	-	-	-	-	-
He I	1.083	$4.23 \pm 0.58$	$3.64 \pm 0.49$	$1.98 \pm 0.27$	$1.99 \pm 0.29$	$2.07 \pm 0.23$	$0.58 \pm 0.09$	-	-
Pa $\beta$	1.282	$0.58 \pm 0.09$	$0.53 \pm 0.08$	$0.62 \pm 0.09$	-	$0.19 \pm 0.31$	$0.15 \pm 0.03$	-	-
[Si X]	1.430	$0.34 \pm 0.05$	$0.25 \pm 0.04$	-	-	-	-	-	-
[Fe II]	1.643	$0.47 \pm 0.06$	$0.46 \pm 0.07$	-	-	-	-	-	-
[Si VI]	1.962	$2.69 \pm 0.35$	-	-	-	-	-	-	-

1, J=3 level  $f_{\nu=1, J=3} = 0.0122$  (Scoville et al. 1982), the H<sub>2</sub> mass was obtained from

$$m_{H_2} \approx 5.0875x10^{13} D^2 I_{1-0S(1)} 10^{0.4277 A_{22}} \quad (2)$$

where D is the distance in Mpc,  $I_{1-0S(1)}$  is the observed flux of H<sub>2</sub>  $\lambda 2.121 \mu\text{m}$  in erg cm $^{-2}$  s $^{-1}$  and  $A_{22}$  is the 2.2- $\mu\text{m}$  extinction calculated through the E(B-V) from Table 4. The mass  $m_{H_2}$  is given in  $M_{\odot}$ .

The results for each aperture are given in Table 5. We have to point here that it is now well known that the distribution of H<sub>2</sub> (perpendicular to the NLR) is so that we miss a large fraction of it in our slit (Sanchez et al. 2009, Galliano et al. 2003). These values are in general agreement with the values obtained by Reunanen et al. (2003) for Seyfert 1 and 2 galaxies, although the nuclear value we obtained is much smaller than what they obtained for NGC 1068. Several reasons may be invoked to explain the difference. The aperture they use to do the analysis is much larger than ours, encompassing all our apertures. As can be seen in Table 4, the extinction varies and the higher values are not in the center. Reunanen et al. probably got an average of these values. In addition, they obtained  $A_{22}$  from the continuum extinction,

**Table 5.** Mass of the excited molecular hydrogen

South	$m_{H_2} [M_{\odot}]$	North	$m_{H_2} [M_{\odot}]$
Ap08	11.8	Ap16	-
Ap07	13.5	Ap15	49.8
Ap06	16.8	Ap14	15.1
Ap05	30.9	Ap13	189.5
Ap04	82.0	Ap12	65.7
Ap03	31.4	Ap11	52.0
Ap02	48.7	Ap10	72.6
Ap01	78.1	Ap09	98.2
Nuc	449.8		

assuming that the difference for the line extinction would not be large. This may be true for many Seyfert galaxies, but the continuum of the nuclear region of NGC 1068 seems to be extremely dusty, as can be seen in Figure 7, by the inclination of the spectrum.

Using the extinction we derived from the emission lines

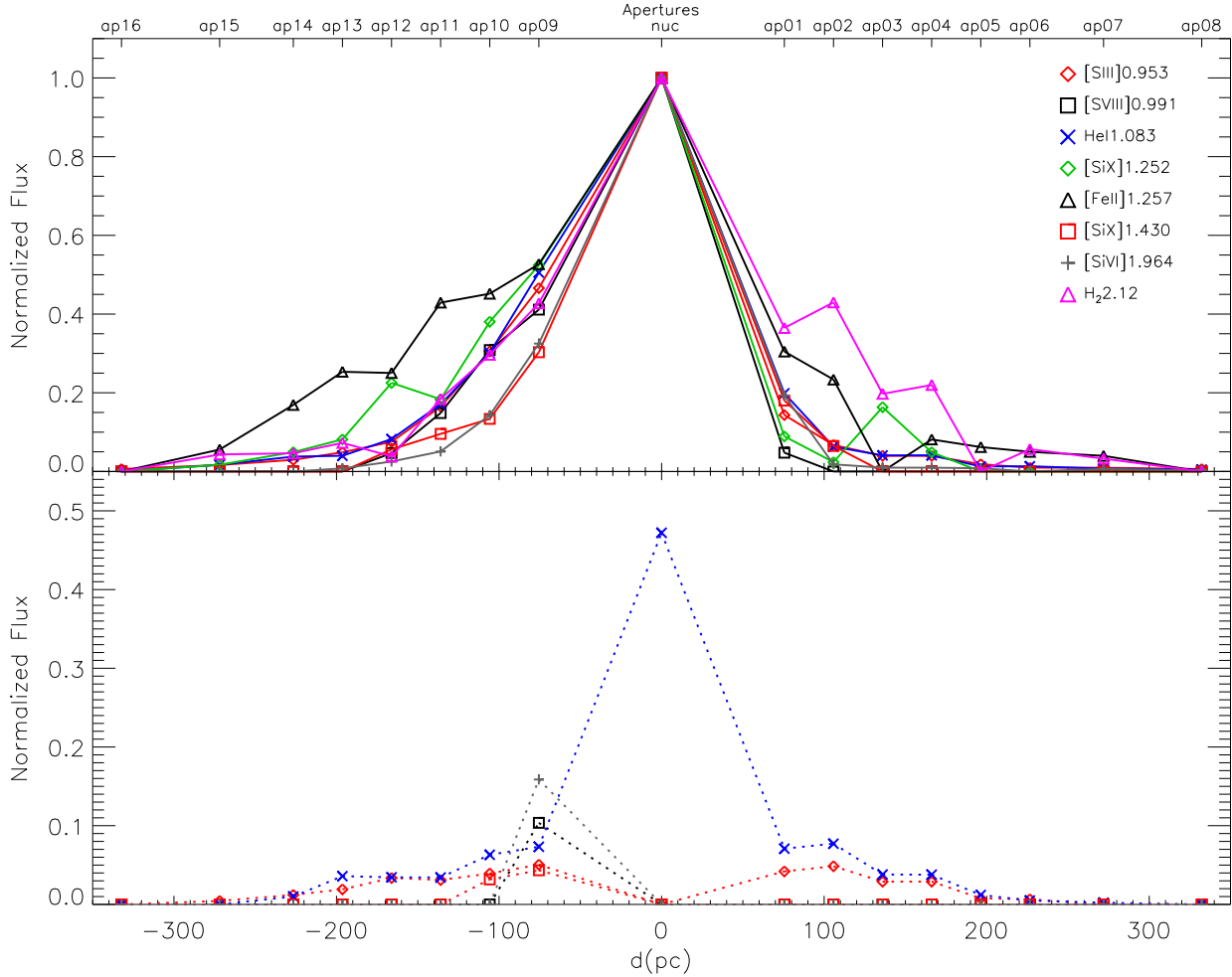


**Figure 10.** Relative flux of main emission lines as a function of the distance to the center. The fluxes were normalized by the center values to allow comparison between lines. Negative distances represent the north direction and positive distances the south. The top panel shows the main components, while the bottom panel shows the second component if present.

(section 4.2) we obtained a much smaller value for the hot molecular gas mass.

#### 4.4 Excitation mechanisms of the $\text{H}_2$ and $[\text{Fe II}]$ lines

Galliano et al. (2003) analyze the possibility of explaining their observations of the MIR emission with diffuse dust in the ionization cone. This model is discarded because the diffuse dust would shield the central engine as well as the BLR from any direction, requiring an ionizing mechanism other than photoionization to explain the NLR emission. On the other hand, they favor a model of thick dust clouds in the cone, with a small covering factor, heated by the central source radiation, without discarding additional heating mechanisms by shocks generated by the interaction of radio jets and gas clouds.

In order to explain the observed molecular emission perpendicular to the cone axis, Galliano et al. (2003) built a numerical model combining a molecular disc and an axisymmetrical, no coplanar, X-ray absorber (see their Figure 9),

reached by X-rays from the central source. This two component model reproduces quite well the main features observed in the  $\text{H}_2$  and CO emission maps.

More recently, the excitation of near infrared  $\text{H}_2$  and Fe II lines have been discussed by Rodríguez-Ardila et al. (2004) based on observations covering the inner 300 pc of most Seyfert galaxies and minimizing contamination by the host galaxy. They showed that the diagnostic diagram  $\text{H}_2\lambda 2.121/\text{Br}\gamma$  versus  $[\text{FeII}]\lambda 1.257/\text{Pa}\beta$  proposed by Larkin et al. (1998) is an efficient tool to separate objects by the level of nuclear activity, i.e., AGN, Starburst or Liner. By including more objects, Rodríguez-Ardila, Riffel & Pastoriza (2005) further test the efficiency of the diagram. For NGC 1068, we obtained  $0.7 < \text{H}_2\lambda 2.121/\text{Br}\gamma < 1.3$  and  $0.6 \leq [\text{FeII}]\lambda 1.257/\text{Pa}\beta \leq 2.8$ . Our results are shown in Figure 12 (filled circles) together with those observed by Rodríguez-Ardila 2004 and 2005 (crosses); the dashed lines show the limits suggested by these authors. The observational data for NGC 1068 corresponding to the nucleus, as well as to different locations along the slit, are in the AGN region of the diagram. This reinforces the results found previously,

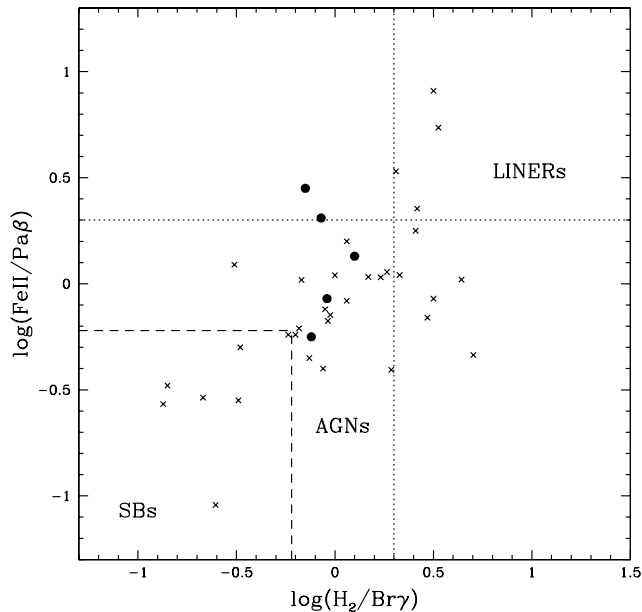


**Figure 12.** Ratios  $H_2$  2.121/ $Br\gamma$  versus  $[Fe II] 1.257 / Pa\beta$ . Filled circles represent our data for NGC 1068. Crosses to data obtained by Rodríguez-Ardila et al. (2004, 2005).

i.e., that this diagram is a helpful tool for classifying objects according to their degree of excitation, and shows that line ratio intensities from slits at different distances from the center can be also used.

In addition, the  $[Fe II]\lambda 1.257 / [P II]\lambda 1.188$  line ratio can be used as a tracer of the ionization mechanism of the emitting gas and depends only on the Fe/P abundance. Following Oliva et al. (2001), in photoionized gas, like HII regions and planetary nebulae, this line ratio is less than 2, while in shock dominated gas its value is higher than 20. The high value would be due to the evaporation of the iron-based grains in the shock front, increasing the Fe abundance relative to P in the low-ionization region. Our data show  $0.70 \leq [Fe II]/[P II] \leq 3.0$ . Such low values might indicate that, either like we mention in section 3.1, the high value of  $[P II]$  observed here might be due to an overabundance of phosphorus, or most of the Fe is locked in grains and the emitting gas is photoionized.

## 5 PHYSICAL CONDITIONS OF THE GAS: NIR CORONAL AND LOW-IONIZATION EMISSION-LINES

In the last few years, photoionization models have been largely used to analyze the physical conditions of the NLR of NGC 1068. Some of these studies tried to reproduce the observed emission-line intensities in a wide wavelength range (Alexander et al. 2000, Kraemer & Crenshaw 2000a, Kraemer & Crenshaw 2000b, Spinoglio et al. 2005), while others were based on selected lines (Groves et al. 2004, Groves et al. 2006, Martins, Viegas & Gruenwald 2003, Rodríguez-Ardila et al. 2006). Recently, Osaki (2009) focus his analysis on the kinematic and excitation structure of the NLR of NGC 1068.

Although the basic photoionization codes used in the literature are very similar, the choice of the input parameters by different authors may change - in particular, the choice of the filling factor. Since one-dimensional photoionization codes are unable to properly deal with an inhomogeneous gas distribution, the optical depth at each cloud shell is multiplied by a chosen filling factor (see, for instance, Osterbrock 1989). The net effect is to increase the size of the low ionized zone as well as to decrease the average temperature of the cloud, which could mislead the conclusions. Following Martins et al. (2003), in the present paper we adopt a multicloud model which should provide a better simulation of the inhomogeneous NLR of NGC 1068.

Another important issue concerning photoionization models is the use of the so-called ionization parameter  $U$  to characterize the intensity of the ionizing radiation continuum. In fact,  $U$  is the ratio of the density of the ionizing photons reaching the cloud to the gas density. It is a convenient free parameter when using diagnostic diagrams to analyze emission-line ratios coming from different galaxies. However, in photoionization models for a given NLR where the distance  $D$  from the ionizing radiation source as well as the source luminosity are known,  $U$  is not a free parameter anymore but it is constrained by the source luminosity, the distance from the ionizing radiation source and the gas density (Ferguson et al. 1997).

As shown in Tables 1, 2 and 3, the main emission line intensities were obtained as a function of the distance to the center. These measured line intensities result from the contribution of all the clouds in the line of sight covered by each aperture. It is not in the scope of this paper to provide a specific model for the observed data from each aperture. Our objective here is to give a scenario to try to explain the observations in general. Thus, in the following, we search for photoionization models which can reproduce the observed range of intensities.

### 5.1 Multi-cloud photoionization model

First attempts to model the emission-line region with a homogeneous gas photoionized by the nuclear radiation failed to reproduce the observed NIR line intensities. As shown below, at least two density regions are necessary to explain the observed data.

In the following, we present a two-cloud model for the NIR emission-lines using the photoionization code Aangaba (Gruenwald & Viegas 1992). The model must reproduce the observed coronal lines  $[SIX]\lambda 1.252$ ,  $[SVIII]\lambda 0.991$ ,  $[SiX]\lambda 1.430$ , and  $[S VI]\lambda 1.962$ , as well as the  $[SIH]\lambda \lambda 0.907$ ,  $0.953$ , and  $[SII]\lambda \lambda 1.032$  emission lines (Tables 1, 2 and 3).

The sulfur line intensity ratios are not directly dependent on the adopted chemical abundance. Thus, they are first used to limit the other input parameters, i. e.,  $U$  (ionization parameter),  $n$  (density) and  $D$  (distance from the ionizing source), given the ionizing radiation luminosity for NGC 1068,  $L_{ion}$ . The model results are then compared to other line ratios, including those for  $[FeXI]\lambda 0.7889$ ,  $[FeX]\lambda 0.6374$ ,  $[FeVII]\lambda 0.6087$  (Rodríguez-Ardila et al. 2006). We assume a solar chemical abundance (Grevesse & Anders 1989).

For NGC 1068, the ionizing radiation luminosity is about  $10^{44.5}$  erg/s assuming a UV power-law index equal

to -1.7 and an X-ray index of -0.5 (Pier et al. 1994, if the reflection factor is 0.01).

In order to fit the high-ionization lines, a large value of  $U$  is usually required. However, due to the relationship between  $U$ ,  $n$ ,  $R$  and  $L_{ion}$ , a high  $U$  requires a low  $n$ , and a low distance from the ionizing source. In the models presented by the different authors referred above, the density value varies from  $10^2 \text{ cm}^{-3}$  (Groves et al. 2006) to  $10^6 \text{ cm}^{-3}$  (Ozaki 2009), although some of them use filling factors as low as  $6.5 \times 10^{-4}$ .

From the observed coronal emission line intensities we note that for gas clouds extending to 200 pc, values of  $U > 0$  are required to fit high-ionization lines, and could be reached only for densities lower than  $10^2 \text{ cm}^{-3}$  (Rodríguez-Ardila et al. 2006, figure 12). After running a series of models for a homogeneous low density gas around the ionizing radiation source, we selected  $n = 1 \text{ cm}^{-3}$  and  $U = 10$  to better fitting the coronal lines; such a model is called model A. The line intensities relative to  $H\beta$  obtained for model A, for an optically thick cloud ( $\tau_{Ly}^A \rightarrow \infty$ ), are given on the second column of Table 6. However, such a model also produces a large semi-ionized region, resulting in a  $[SIII]/[SII]$  line ratio too high. Thus the final model for the low density gas should be matter bound (see below).

While the coronal line ratios are more sensitive to the  $U$  parameter, the  $[SIII]/[SII]$  line intensity ratio is more dependent on the gas density. The observed values indicate that densities  $10^6 \text{ cm}^{-3}$  or higher are required to reproduce the observed line ratio. Notice that high density clouds ( $10^{5.3} \text{ cm}^{-3}$ ) are also favored by Ozaki (2009) when modeling the structure of the NLR of NGC 1068 using the optical emission-lines  $[FeVII]$ ,  $[OIII]$ , and  $[OI]$ , relative to  $H\beta$ . Thus, we assume that high density clouds ( $10^6 \text{ cm}^{-3}$ ) are radiation bound, located farther from the central source and being shielded from the UV, but not from the X-ray, by the low density gas producing the coronal lines. The results for a model using an ionizing spectrum with  $E \geq 200 \text{ eV}$  are shown in Table 6 (model B). In addition to  $[SIII]$  and  $[SII]$  lines, this high density gas produces also the  $[SiVI]$  emission line, but not the other coronal lines as expected.

The high density clouds contribute mainly to the low ionization emission lines. In order to obtain the fraction  $f$  of the contribution of the high density clouds relative to the coronal gas, we use the  $[SVIII]/[SIII]$  observed line ratios (Table 1, 2 and 3). Since  $[SIII]$  comes both from models A and B, such line ratio depends on the optical depth at the Lyman limit of the low density region. As noticed above, the  $[SiVI]$  line could partially come from the high density clouds. However their contribution is much smaller than that from the low density region, so that the  $[SiX]/[SiIV]$  ratio is practically independent of  $f$ . As said above, the low density cloud must be matter bound for not emitting too much  $[SII]$  or  $[SIII]$ . The best results are obtained with  $\tau_{Ly}^A$  for model A between 1 and 5. In Table 6, the line intensity ratios for  $\tau_{Ly}^A = 5$  and 1 are listed (third and fourth columns, respectively). For  $\tau_{Ly}^A$  of model A equal 1 and 5, the corresponding fractions  $f$  are equal to 0.078 and 0.065, respectively, leading to a luminosity ratio of  $H\beta$  between the two components equal to 10.2 and 38.7. The range of the observed infrared line ratios is shown in Table 7, compared to the results of the two possible two-cloud models, i. e., the combination of model

**Table 6.** Line intensities for components A and B, relative to  $H\beta$

	mod A $\tau_{Ly}^A \rightarrow \infty$	mod A $\tau_{Ly}^A=5$	mod A $\tau_{Ly}^A=1$	mod B $\tau_{Ly}^B \rightarrow \infty$
$[SII]/H\beta$	3.5E-3	6.2E-5	9.2E-6	7.6E+0
$[SIII]/H\beta$	9.1E-1	4.2E-1	9.1E-2	7.1E+1
$[SVIII]/H\beta$	3.2E-2	4.5E-2	1.4E-1	0.0E+0
$[SIX]/H\beta$	7.9E-2	1.1E-1	3.5E-1	0.0E+0
$[SiVI]/H\beta$	6.6E-2	9.1E-2	2.5E-1	4.2E-5
$[SiX]/H\beta$	2.1E-2	2.9E-2	9.0E-2	0.0E+0
$[FeVII]/H\beta$	1.1E-1	1.5E-1	4.5E-1	0.0E+0
$[FeX]/H\beta$	4.9E-2	6.8E-2	2.2E-1	0.0E+0
$[FeXI]/H\beta$	2.2E-2	3.1E-2	9.7E-2	0.0E+0

**Table 7.** Results for the multi-cloud model (in logarithm)

	observation	multi-cloud model $\tau_{Ly}^A=1$ $\tau_{Ly}^A=5$	
$[SIII]/[SII]$	+0.8 to +1.2	+1.0	+1.1
$[SVIII]/[SIII]$	-2.0 to -1.5	-1.7	-1.7
$[SIX]/[SIII]$	+0.0 to +0.7	+0.4	+0.4
$[SiX]/[SiVI]$	-0.4 to +0.0	-0.4	-0.5
$[FeX]/[FeVII]$	-0.5 to -0.4	-0.3	-0.3
$[FeXI]/[FeX]$	-0.9 to -0.2	-0.4	-0.4

B with model A (for  $\tau_{Ly}^A = 1$  and 5). Notice that detailed models for each aperture may require a range of densities.

All line ratios are in the range of the observational data (Tables 1, 2 and 3), including the coronal iron lines from Rodríguez-Ardila et al. (2006). In that paper, only models with density  $\geq 10^3 \text{ cm}^{-3}$  were used, and pure photoionization models could not reproduce the line ratios. Here we relax this lower limit, and most of the ratios could be reproduced. This, however, does not discard the possibility of having other ionization mechanisms playing a role. To put a stronger constrain on this issue it would be necessary to fit a large amount of emission-lines in a broader range of wavelengths, which is out of the scope of this paper.

## 6 THE CENTRAL MASS

We have used the stellar absorption features to estimate the mass of the central region inside the extraction apertures. The velocity dispersion was estimated using the same velocity distribution and methodology proposed by Van der Marel & Franx (1993). The  $h3$  and  $h4$  coefficients, which measure the distortions from a gaussian distribution, are very uncertain and therefore we restrict our discussion to the velocity dispersions. The results were obtained using as template a mixture of standard stellar spectra with the same resolution as our nuclear spectra of NGC1068 and high S/N. The spectral region was the same used by Tamura et al. (1991) for this same galaxy, around  $2.26 \mu\text{m}$ , where there are strong molecular absorptions due to CO. This region seems adequate since the interstellar absorption is small and there are no emission lines. Errors in the velocity dispersions were obtained using the S/N of the spectra. An example of the fit is shown in Figure 13.



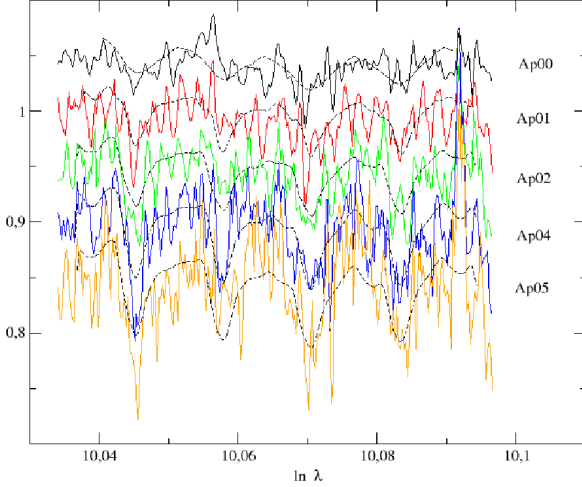


**Figure 13.** Example of the fitting process. Color lines represent the observed spectra and dashed black lines are the adjusted model.

The results are shown in Figure 14 and we can observe that the velocity dispersion rises strongly in the central region, probably due to the AGN contribution. Moreover in this very central region the light contribution of the AGN and the hot dust contaminates the stellar continuum and makes it difficult to measure the velocity dispersion. Away from the center the nuclear contamination is much lower in our extracted spectra and we observe that the velocity dispersion remains quite large for a typical spiral galaxy. Nevertheless moving outwards to 100 pc from the nucleus the velocity dispersion is quite close to the values already reported in the literature.

Using these determinations and the Virial theorem we give a very crude estimate showing how the central mass depends on the adopted nuclear distance. Our approach consists in using a simple model that can be resolved analytically and compared to the data. Basically the model consists of an stellar core with uniform density,  $\rho_*$ , extending to a maximum radial distance  $R_*$ . The total mass of this stellar core is  $M_*$  and in the central region we add a punctual mass,  $M_0$ , that simulates the presence of the AGN and its accretion disk. The total mass profile can be readily estimated as

$$M(R) = M_* \left( \frac{R}{R_*} \right)^3 + M_0 \quad (3)$$

where  $R$  represents the radial distance. Assuming that the velocity distribution of the stellar component is random and isotropic we derive that

$$\sigma_v^2(R) \approx GM_* \left( \frac{1}{5} \frac{R^2}{R_*^3} + \frac{\gamma}{3} \frac{1}{R} \right) \quad (4)$$

where  $\sigma_v^2(R)$  is the velocity dispersion and  $\gamma = M_0/M_*$  is a measure of the relative importance of the central mass compared with the core stellar distribution. However we only have access to the average kinetic energy of the stars projected in the line of sight of the observer. Weighting this component by its luminosity contribution, or by mass for a constant mass-luminosity ratio, we have

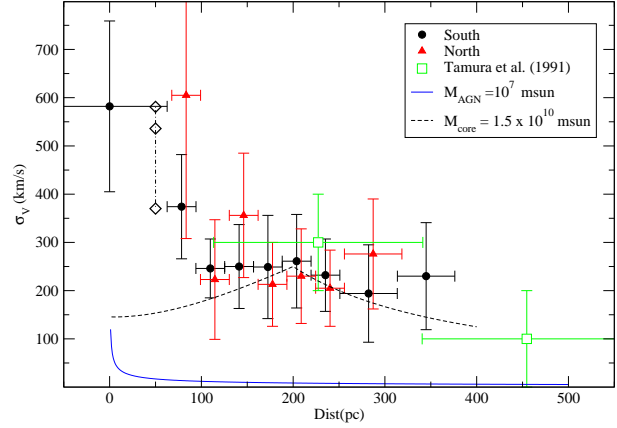


**Figure 14.** Core model applied to NGC 1068

$$\sigma_{v,obs}^2(r) = \frac{\int_0^L \sigma_v^2(R) \rho(R) dl}{\int_0^L \rho(R) dl} \quad (5)$$

and assuming that the density of the stellar core is uniform, we finally obtain our estimation for the observed line of sight velocity dispersion as

$$\sigma_{v,obs}^2(r) = \frac{\sigma_{v,obs}^2(R_*)}{3 + 5\gamma} \left[ 1 + 2 \frac{r^2}{R_*^2} + \frac{5\gamma}{(1 - r^2/R_*^2)^{1/2}} \sinh^{-1} \left( \frac{R_*^2}{r^2} - 1 \right)^{1/2} \right] \quad (6)$$

For large values of  $\gamma$  the central mass dominates and we simply have a keplerian profile which is shown as the blue continuous curve in Figure 14. We can see that the observed profile is completely inconsistent using the usual BH mass estimation ( $\simeq 1 - 2 \times 10^7 M_\odot$ ) found in the literature (Lodato & Bertin 2002). To explain the high velocity dispersion of 255 km/s in the central region we need to include an stellar core of  $1.5 \times 10^{10} M_\odot$  extending to approximately 200 pc from the nucleus shown as the dotted line. Therefore a value  $\gamma = 6.6 \times 10^{-4}$  would be a more appropriated contribution of the central mass.

## 7 SUMMARY AND CONCLUSIONS

We carried out long-slit spectroscopy in the Near-IR of NGC 1068 and presented here for the first time the whole range from 0.9 to 2.4  $\mu\text{m}$ , extending 15" in the nuclear region. The nuclear emission shows many important emission lines, from low ionization to coronal lines, molecular lines and absorption features. We show that many emission lines are composed by two narrow components, one in the galaxy rest frame, and the other blueshifted in the south and redshifted in the north apertures. The relative intensity of the peaks also varies and they seem to be correlated with the jet of the galaxy. No broad component ( $\sim 2000$ ) was identified in any line profile. Not all emission lines have double peaked profiles and some lines are present only near the center, particularly the high ionization lines. This is a clear indication that the emitting gas is more ionized in the nuclear region.

We estimated the extinction based on Paschen hydrogen

and [FeII] emission lines. E(B-V) is highest in the nucleus then in the adjacent regions, but there are peaks around 150 - 200 pc from each side of the nucleus. This is also close to the region where the second components of the emission lines have a maximum, and may be associated with dense clouds around these regions. H<sub>2</sub> emission is very extended, but it is difficult to identify the ionization process because only the 1-0(S1) line could be measured.

Simple photoionization models were used to try to explain the emission lines, and a first approximation shows that the line ratios can be explained with pure photoionization, as long as low density clouds are present. A more detailed analysis however is necessary, to rule out other ionization mechanisms.

We also used the stellar signatures to determine the mass of the central region, obtaining a stellar core of  $1.5 \times 10^{10} M_{\odot}$ .

## ACKNOWLEDGMENTS

This research has been partially supported by the Brazilian agency FAPESP (2007/04316-1). ARA acknowledges partial support of CNPq through grant 308877/2009-8. The authors would like to thank Dr. Sueli Viegas for the helpful insights and comments on the paper. We also thank the anonymous referee for valuable comments. The IRS was a collaborative venture between Cornell University and Ball Aerospace Corporation funded by NASA through the Jet Propulsion Laboratory and Ames Research Center.

## REFERENCES

- Alexander, T., Lutz, D., Sturm, E., Genzel, R., Sternverg, A., & Netzer, H. 2000, *ApJ*, 536, 710
- Alloin, D., Pelat, D., Boksenberg, A., & Sargent, W.L.W. 1983, *ApJ*, 275, 493
- Alloin, D., Pantin, E., Lagage, P.O., & Granato, G.L. 2000, *A&A*, 363, 926
- Antonucci, R.R.J., & Miller, J.S. 1985, 297, 621
- Axon, D.J., Marconi, A., Capetti, A., Macchetto, F.D., Schreier, E., & Robinson, A. 1998, *ApJ*, 496, L75
- Bautista, M.A. & Pradhan, A.K. 1998, *ApJ*, 492, 650
- Bicknell, G., Dopita, M.A., Tsvetanov, A.I., & Sutherland, R.S. 1998, *ApJ*, 495, 680
- Cardelli, J.A., Clayton, G.C., Mathis, J.S. 1989, *ApJ*, 345, 245
- Cecil, G., Bland, J., & Tully, R.B. 1990, *ApJ*, 355, 70
- Cecil, G., Dopita, M.A., Groves, B., Wilson, A.S., Ferruit, P., Pécontal, E., & Binnet, L. 2002, *ApJ*, 568, 627
- Cid Fernandes, R., Heckman, T., Schmitt, H., González Delgado, R., & Storchi-Bergmann, T. 2001, *ApJ*, 558, 81
- Crenshaw, D.M. & Kraemer, S.B. 2000a, *ApJ*, 532, 247
- Crenshaw, D.M. & Kraemer S.B. 2000b, *ApJ*, 532, L10
- Cushing, M.C., Vacca, W.D., & Rayner, J.T. 2004, *PASP*, 116, 362
- Dopita, M.A. & Sutherland, R.S. 1996, *ApJS*, 102, 161
- Evans, I.N., Ford, H.C., Kinney, A.L., et al. 1991, *ApJ*, 369, L27
- Ferguson, J.W., Korista, K. T., & Ferland, G. J. 1997, *ApJS*, 110, 287
- Galliano, E., Alloin, D., Granato, G.L., & Villar-Martín, M. 2003, *A&A*, 412, 615
- Gallimore, J.F., Baum, S.A., O’Dea, C.P., & Pedlar, A. 1996, *ApJ*, 458, 136
- Grevesse, N., & Anders, E. 1989, in *AIP Conf. Proc.* 183, Cosmic Abundances of Matter (New York: AIP), 1
- Groves, B.A., Cecil, G., Ferruit, P., & Dopita, M.A. 2004, *ApJ*, 611, 786
- Groves, B., Dopita, M., & Sutherland, R. 2006, *A&A*, 458, 405
- Gruenwald, R., & Viegas, S. M. 1992, *ApJS*, 78, 153
- Higdon, S.J.U., Devost, D., Higdon, J.L., et al. 2004, *PASP*, 116, 975
- Ivanov, V.D., Rieke, G.H., Groppi, C.E., Alonso-Herrero, A., Rieke, M.J., & Engelbracht, C.W. 2000, *ApJ*, 545, 190
- Kraemer, S. B., & Crenshaw, D. M. 2000a, *ApJ*, 532, 256
- Kraemer, S. B., & Crenshaw, D. M. 2000b, *ApJ*, 544, 763
- Kraemer, S.B., Ruiz, J.R., & Crenshaw, D.M. 1998, *ApJ*, 508, 232
- Larkin, J. E., Armus, L., Knop, R. A., Soifer, B. T., & Matthews, K. 1998, *ApJS*, 114, 59
- Lodato & Bertin 2002
- Macchetto, F., Capetti, A., Sparks, W.B., Axon, D.J., Boksenberg, A. 1994, *ApJ*, 435, 15
- Martins, L.P., Viegas, S.M. & Gruenwald, R. 2003
- Martins, L.P., Riffel, R., Ardila, A., Gruenwald, R., de Souza, R. 2010, submitted to *MNRAS*
- Mazzalay, X. & Rodríguez-Ardila, A. 2007, *A&A*, 463, 445
- Meaburn, J. & Pedlar, A. 1986, *A&A*, 159, 336
- Myers, S.T., & Scoville, N.Z. 1987, *ApJ*, 312, 39
- Nussbaumer, H. & Storey, P.J. 1988, *A&A*, 193, 327
- Oliva et al. 2001, *A&A*, 369, L5
- Origlia, L., Moorwood, A.F.M., Oliva, E. 1993, *A&A*, 280, 5360
- Osaki, S. 2009, *PASJ*, 61, 259
- Osterbrock, D.E. 1989, *Astrophysics of Gaseous Nebulae and Active Galactic Nuclei* (Mill Valley: University Science Books)
- Pelat, D. & Alloin, D. 1980, *A&A*, 81, 172
- Pier, E.A., Antonucci, R., Hurt, T., Kriss, G., & Krolik, J. 1994, *ApJ*, 428, 124
- Pogge, R.W. 1988, *ApJ*, 328, 519
- Rayner, J.T., Toomey, D.W., Onaka, P.M., Denault, A.J., Stahlberger, W.E., Vacca, W.D., Cushing, M.C., & Wang, S. 2003, *PASP*, 155, 362
- Reunanen, J., Kotilainen, J.K., & Prieto, M. A. 2003, *MNRAS*, 343, 192
- Rodríguez-Ardila, A., Pastoriza, M.G., Viegas, S., Sigut, T.A.A., & Pradhan, A.K. 2004, *A&A*, 425, 457
- Rodríguez-Ardila, A., Riffel, R., & Pastoriza, M. G. 2005, *MNRAS*, 364, 1041
- Rodríguez-Ardila, A., Prieto, M. A., Viegas, S., & Gruenwald, R. 2006, *ApJ*, 653, 1098
- Schinnerer, E., Eckart, A., & Tacconi, L.J. 1998, *ApJ*, 500, 147
- Schreiber, A.W.
- Scoville, N.Z., Hall, D.N.B., Keinmann, S.G., & Ridgway, S.T. 1982, *ApJ*, 253, 136
- Spinoglio, L., Malkan, M. A., Smith, H. A., Gonzalez-Alfonso, E., & Fischer, J. 2005, *ApJ*, 623, 123
- Tacconi, L.J., Genzel, R., Blietz, M., Cameron, M., Harris, A.I., Madden, S. 1994, *ApJ*, 426, 77
- Tamura, M., Kleinmann, S.G., Scoville, N.Z., & Joyce, R.R. 1991, *ApJ*, 371, 131
- Telesco, C.M., & Decher, R. 1988, *ApJ*, 334, 573
- Thatte, N., Quirrenbach, R., Maiolino, R., & Tecza, M. 1997, *ApJ*, 490, 238
- Tully 1988
- Turner, J., Kirby-Docken, K., & Dalgarno, A. 1977, *ApJS*, 35, 281
- Unger, S.W., Lewis, J.R., Pedlar, A., Axon, D.J. 1992, *MNRAS*, 258, 371
- Vacca, W.D., Cushing, M.C. & Rayner, J.T. 2003, *PASP*, 115, 389
- Van der Marel, R.P. & Franx, M. 1993, *ApJ*, 407, 525
- Veilleux, S., Goodrich, R.W., & Hill, G.J. 1997, *ApJ*, 477, 631

Wilson, A.S. & Ulvestad, J.S. 1983, ApJ, 275, 8

Zheng, W., Wang, J-X., Kriss, G.A., Sahnou, D., Allen, M., Dopita, M., Tsvetanov, Z., Bicknell, G. 2008, ApJ, 686, 881

This paper has been typeset from a T<sub>E</sub>X/ L<sup>A</sup>T<sub>E</sub>X file prepared by the author.